Systemic loss of Sarm1 is glioprotective after neurotrauma

Weili Tian*, Amir Asgharsharghi*, Gema Valera*, Tim Czopka§, Melanie Haehnel-Taguchi# and Hernán López-Schier*

* Sensory Biology & Organogenesis, Helmholtz Zentrum Munich, Germany

§ Institute of Neuronal Cell Biology, Technical University of Munich, Germany

Institute of Biology I, Albert Ludwigs University, Freiburg, Germany

Correspondence to: Dr. Hernán López-Schier

E-mail: hernan.lopez-schier@helmholtz-muenchen.de

Abbreviated title: Sarm1 and glioprotection

Number of figures and tables:

Number of pages:

Total number of words:

Keywords: Wallerian degeneration, Sarm1, Schwann cells, regeneration

Acknowledgements: We thank M. Wagner and J. Winkelmann for advice. This research was supported by a Grant from the Human Frontiers Science Programme and by the Helmholtz Gemeinschaft to H.L-S.

ABSTRACT

Protecting the nervous system from chronic effects of physical and chemical stress is a pressing clinical challenge, which has sparked intense efforts to identify molecular inhibitors of axon destruction. Yet, one caveat of such strategy is the extent of unintended deleterious effects of blocking axon degeneration systemically. Here we use genetics and pharmacology in zebrafish to show that elimination of the obligate pro-degenerative protein Sarm1 is compatible with neural homeostasis and function, and is glioprotective. Severed axons lacking Sarm1 subsist independently of Schwann-cell support. Regenerating axons in Sarm1 mutants do not reseal with non-degradable axon segments and regain connectivity with peripheral synaptic targets to enable sensorimotor recovery, suggesting that neural-circuit repair is not contingent upon expeditious clearance of damaged axons. Unexpectedly, we found that Sarm1 deficiency increases Schwann-cell resistance to toxicity by diverse chemotherapeutic agents after nerve injury. Our findings anticipate that pharmacological interventions targeting Sarm1 are promising strategies to reduce chronic consequences of neurotrauma.

INTRODUCTION

The peripheral nerves that communicate skin, muscle and sensory organs with the brain must maintain functionality throughout life despite frequent stress and trauma (1-6). Loss of integrity of peripheral neurons and associated cells, including glia, is a common occurrence in severe neurological dysfunctions that include weakness, pain and loss of sensation (7). Glial loss leads to nerve demyelination, defasciculation, and eventual neuronal death. Neuronal injury triggers the swelling of axons and synaptic disengagement, followed by axon fragmentation and degeneration. Axonal loss also induces dedifferentiation of associated glial cells. This enhances glial functional role in clearing axon fragment and aid in nerve repair, but also makes them vulnerable to degeneration after protracted denervation (8-12). Damaged axons undergo Wallerian degeneration (13). This type of active axon degradation is regulated by the evolutionary-conserved pro-degenerative protein Sarm1 (Sterile Alpha and TIR Motif containing 1) (14-17). Sarm1 is a modular protein that contains two sterile-alpha motifs (SAM), one mitochondrial association (MT) and one TIR domain (14). Nerve injury activates Sarm1 by TIR dimerization, which is sufficient to induce the degeneration of the affected axons (18, 19). Mechanistically, Sarm1 activation results in the loss of nicotinamide adenine dinucleotide (NAD+) in damaged axons, which ultimately underlies their destruction (20-22). The TIR domain acts as a NADase (23), explaining why over-expression of the NAD+ synthesizing enzyme NMNAT1 inhibits the degradation of severed axons by sustaining high levels of NAD+ downstream of Sarm1 (24). Moreover, experiments in *Drosophila* and mammalian neurons have shown that the loss of Sarm1 blocks the degeneration of severed axons, and that forced

activation of Sarm1 induces axon destruction in the absence of injury. Therefore, Sarm1 is a discrete hierarchical regulator of a signaling pathway that is necessary and sufficient for axon degradation (22).

Upon peripheral nerve injury, glial Schwann cells dedifferentiate to acquire a specialized function that promotes the clearance of axon fragments ahead of axonal re-growth from the proximal stump that remains associated to the neuronal perikaryon (25). Expeditious axonal regeneration is important because sustained Schwann-cell denervation leads to protracted loss of glial terminal phenotype and eventual death. In turn, glial loss impairs regenerating nerve myelination and circuit repair, transforming acute neuropathies into irreversible chronic neurological dysfunction. Therefore, inhibiting or delaying axon destruction has been hypothesized as an effective strategy to counter heightened Schwann-cell vulnerability to additional stressors that include metabolic imbalance and drugs (26, 27). This idea has sparked intense academic and commercial efforts to identify specific molecular inhibitors of axon degeneration for clinical applications (28, 29). However, the effectiveness and applicability of such strategy depend on the extent of potentially deleterious effect of blocking axon degeneration chronically and systemically. This is important because it remains unclear whether blocking axonal destruction may affect physiological axonal dynamics, including neurite retraction and shedding that are naturally occurring phenomena during refinement of neuronal circuits (30). Also, whether the maintenance of damaged axons may impair the reconstruction of neuronal circuits during normal wear and tear. For instance, normal aging delays Wallerian axon

degeneration, impairing Schwann-cell reparative responses after nerve injury (31).

Here we address the above issues in zebrafish, a small vertebrate whose nervous system is anatomically simpler but structurally and functionally equivalent to that of mammals (32-34). Crucially, the zebrafish larva is ideal to study axonal degeneration and regeneration, and Schwann-cell biology in the natural context of the behaving animal (35-42). To systemically eliminate Wallerian axon degeneration, we generated loss-of-function mutations in Sarm1 (15, 43). We combined microsurgery, multicolor high-resolution intravital microscopy, electrophysiology, pharmacology and behavioral tests to provide novel insights into the cellular basis of axon degradation and nerve repair. Our findings encourage the quest to identify and develop specific Sarm1 inhibitors for clinical application.

RESULTS

Identification and mutagenesis of Sarm1 in zebrafish

The amino-acid sequence of Sarm1 is well conserved across species (15). To identify Sarm1 orthologs in zebrafish, we scanned publicly accessible genomic data (*Danio rerio* reference genome assembly version GRCz11) by a BLAST search using the TIR domain, which is present in all known Sarm1 proteins (15, 44). This exploration yielded a single candidate *locus* in chromosome 15. No other part of the zebrafish genome appears to harbor Sarm1 paralogs. The genomic structure of the putative zebrafish Sarm1 reminisces that of other species, containing 8 exons that code for a

protein of 713 amino acids (Figure 1A-B), with the typical N-terminal auto-inhibitory domain, two central SAM multimerization domains and a C-terminal TIR degeneration domain (Figure 1B). Similarly to *Drosophila*, however, zebrafish Sarm1 lacks an obvious mitochondria-targeting sequence (MT). To test whether the identified gene produces a protein with the expected functional role, we used CRISPR/Cas9-mediated genome modification to generate loss-of-function mutations in Sarm1. By targeting exon 1 (Figure 1C), we obtained germ-line transmission of two alleles: *sarm1*^{hzm13} and *sarm1*^{hzm14} (Figure 1D). The hzm13 allele introduces an 11-base deletion and T/C mutation, resulting in a frame shift and premature stop codon that is likely to generate a truncated protein lacking all the domains with known function. hzm14 is a 7-base deletion and AG/GA mutation that also generates a frame shift and premature stop codon. Analysis of protein extracts from wild-type embryos by Western-blot using an antibody to Sarm1 revealed a single band of approximately 80kDa, which agrees with the expected size of the full-length protein (Figure 1E). This band was absent in protein extracts from homozygous *sarm1*^{hzm13} zebrafish embryos. Homozygous mutant larvae display no overt anatomical defects (Figure 1F-G), are viable and develop into fertile adults (not shown). A simple assay for sensorimotor function that consists of eliciting the escape response after tactile stimuli showed that the displacement distance and the average acceleration were no different between wild-type and Sarm1 mutant specimens (Figure 1H-I) (45). We decided to conduct all additional studies using homozygous *sarm1*^{hzm13}.

Sarm1 is dispensable for the development and maintenance of a sensorineural pathway

To assess the effects of systemic loss of Sarm1 on the nervous system we used several parameters of neuronal structure and circuit function by combining *sarm1*^{hzm13} with various transgenes expressing fluorescent markers in the afferent neurons of the mechanosensory lateral line, as well as in their associated Schwann cells (46, 47). The lateral-line system is ideal for *in vivo* studies at high resolution over extended periods, and for physiological studies under normal and altered conditions (48-51). It combines the organization of a typical vertebrate sensory system with the amenability for controlled experimental interventions that include microsurgery, pharmacology and optogenetics (41, 42, 52, 53). Additionally, the lateral line mediates a robust behavioral reaction to water currents called rheotaxis, which can be easily quantified by measuring the orientation of the animal to the direction of water flow (54-56).

We found that loss of Sarm1 does not affect the development and maintenance of the lateralis sensory pathway (Figure 2A-G). Lateralis afferent ganglia appear of normal size localization in the head of the fish (Figure 2A-B). Lateralis neurons are correctly polarized, projecting peripheral axons that arborize normally underneath the receptive peripheral organs called neuromasts (Figure 2C-D) (46). Additionally, neuronal central projections along the length of the ipsilateral hindbrain are structurally (Figure 2E-F) and numerically (Figure 2G) indistinguishable from age-matched wild-type controls. Next, we assessed neuronal intracellular dynamics and physiological function. To this end, we fluorescently marked mitochondria in lateralis

neurons by expressing the mitochondria targeting sequence of the Cytochrome-C oxidase subunit 8A fused to mCherry (57). We chose mitochondria because mitochondria produce energy for the neurons and also regulate calcium levels, which are critical for the function and viability of axons and neurons. These intracellular organelles are dynamic and distribute throughout the neuron by active transport mediated by molecular motors that move along microtubule tracks. In axons, microtubules are polarized such that their plus ends are directed toward the axon terminals, in turn orienting the movement of distinct molecular motors in the antero- and retro-grade directions (58). Intra-axonal movement direction also reflects mitochondrial fitness because stressed organelles are biased in the retrograde direction (59, 60). Therefore, axonal mitochondria represent an optimal proxy for neuronal polarization, intracellular dynamics and overall cellular health. We found a qualitatively similar number, density and distribution of mitochondria in the peripheral axons of wild type and Sarm1 mutants (Figure 2H-I). Kymographic analysis revealed a majority of static large mitochondrial groups, and some smaller fragments moving persistently substantial distances at constant velocity in the anterograde and retrograde directions (Figure 2J). Importantly, quantifications showed no significant differences in the number and spatial distribution of axonal mitochondria (Figure 2K), or movement velocity and direction (Figure 2L) between wild-type and mutant animals.

Having established that the structure of this sensory system is not affected by the loss of Sarm1, we tested its function using a sensitive assay consisting of a 100-millisecond

mechanical stimulation of neuromasts with a water jet and loose patch recordings from lateralis afferent neurons (54). This experiment showed spontaneous and evoked neuronal activity in Sarm1 mutant and control larvae (Figure 3A). Although, in general spontaneous spike rate and spike amplitude can vary across recordings from lateralis afferent neurons, it appears that spike amplitude is lower in Sarm1 mutants compared to controls (61). Raster plots from two stimulus protocols in control and Sarm1 larvae show that both reliably respond to repeated stimulation (Figure 3B). The spontaneous spike rates of lateralis neurons (Figure 3C) and the latency of response onset after stimulus presentation (Figure 3D) were not significantly different between control and mutants. Both, Sarm1 and control larvae respond with a significant increase in the spike rate to mechanical stimulation, however there was no significant difference in response strength between Sarm1 mutants and controls (Figure 3E). We next asked whether these mild differences of neuronal activity might impact the behavioral reaction of the fish to water flow that is mediated by the lateral line (55, 56). We conducted a rheotactic assay by exposing larval zebrafish to 6mm/s laminar water flow and measure their orientation to flow direction. We found that rheotaxis by normal specimens was only marginally better than that of Sarm1-deficient animals (Figure 3F). Together, these data indicate that Sarm1 is a non-essential gene whose systemic loss is compatible with life, normal growth, reproduction, and nervous system development and function in zebrafish.

Sarm1 is essential for the degradation of severed axons in zebrafish

Loss of Sarm1 in *Drosophila* and the mouse prevent the degradation of injured axons (15, 62). To test functional conservation of Sarm1 in zebrafish, we used a previously established bioassay of neurotrauma in the lateral line (63). The preparation employs intact larval zebrafish, laser-mediated severing of axons individualized by single-cell fluorescent-protein expression, and intravital high-resolution videomicroscopy of axons and their associated Schwann cells (41). Axotomy was done in fluorescently marked neurons by focusing an ultraviolet laser beam to a discrete region of the peripheral axons. Upon severing, the distal axon segment quickly degenerates in wild-type specimens, whereas the proximal segment that remains associated with the neuronal perikaryon remains intact (Figure 4A). However, severed axons in Sarm1 mutants do not degenerate (Figure 4B). Kinetic analysis shows that wild-type axons degenerate following two phases: a fragmentation of the distal part that starts as soon as 2 hours-post-injury (hpi), and a complete clearance that can be completed as early as 8 hpi (Figure 4C). By contrast, severed Sarm1-deficient axon segments resisted degeneration for over 5 days (Figure 4C). The degeneration-resistant phenotype was rescued by the transgenic introduction of a fluorescent-tagged full-length Sarm1 in mutant neurons (Figure 4D). We found that axon degeneration and clearance is cell-autonomous, because the co-existence of Sarm1(+) and Sarm1(-) axons does not interfere with the maintenance of severed mutant axons and the degeneration of those having a functional Sarm1 (Figure 4D).

In *C. elegans* worms, severed axons of mechanosensory neurons reseal with the proximal stumps to quickly repair the neuronal pathway (64, 65). Whether axon

resealing occurs in other species remains unknown. We asked if the strongly delayed axon degradation in Sarm1 mutant zebrafish to would favor axon resealing. To recognize the distal and proximal segments of the same axon after severing and during re-growth, we expressed in individual lateralis neurons the fluorescent protein Kaede, which can be photoconverted with blue light from its initial green fluorescence (Kaede_G) to red fluorescence (Kaede_R) (66). Individual Kaede_G-expressing axons in Sarm1 mutants were transected, and immediately afterwards the distal segments were illuminated for a short period to render them red fluorescent (Figure 4E). Samples were kept in the dark and imaged 14 hpi to assess resealing. In no instance did we see fusion events between the proximal (Kaede_G) and distal (Kaede_R) axon segments (Figure 4F-G). Proximal axons, instead, grew past the non-degradable distal segments to re-innervate the neuromasts (Figure 4F).

Equivalent sensorimotor recovery after nerve regeneration in wild-type and Sarm1 mutant zebrafish

We used the natural regeneration of the lateralis peripheral nerve to test the impact of systemic loss of Wallerian axon degeneration on sensorimotor recovery after damage. Unilateral abrogation of anterior and posterior lateral-line function completely eliminates rheotaxis under laminar flow (56). Therefore, we severed all peripheral axon of the anterior and posterior lateral line on one side of larval zebrafish and tested rheotaxis 1 and 3 days afterwards, respectively 1 and 3 dpi. We confirmed that without lateral-line input 1 dpi, rheotaxis was severely disrupted in wild-type and Sarm1-mutant larvae (Figure 4H), and found that rheotaxis partially recovered 3 dpi,

with no significant difference between wild type and Sarm1 mutants. Taken together, these results indicate that the maintenance of severed axons in Sarm1-mutant animals does not affect the re-innervation of sensory receptors by regenerating axons, or restoration of sensory function after circuit repair.

Synthetic elevation of intracellular calcium suffices to induce the degradation of severed Sarm1-deficient axons

Calcium regulation in neurons is critical for homeostasis because sustained elevation of cytosolic calcium leads to axonal and neuronal degeneration. Often, this occurs because mitochondria release apoptosis-inducing factors and proteases in a calcium-dependent manner (67). Studies of mammalian neurons *in vitro* and of zebrafish have shown that neuronal damage triggers two waves of elevation of axoplasmic calcium (Ca^{2+}) (21, 52). The first occurs nearly immediately after injury and decays rapidly, whereas the second has slower onset and decay. Loss of Sarm1 prevents Ca^{2+} elevation in severed axons (21). We sought to further test the functional conservation of Sarm1 in zebrafish *in vivo* by monitoring Ca^{2+} dynamics in lateralis sensory axons at high-resolution before and after injury. To this end, we expressed the Ca^{2+} fluorescent sensor GCaMP7a in wild-type and Sarm1-mutant lateralis neurons and assessed green fluorescence by fast intravital videomicroscopy at 2.5 Hertz (Figure 5A) (68). Undamaged wild-type and Sarm1-mutant axons show undetectable levels of axoplasmic fluorescence above background (Figure 5A). Upon severing, fluorescent signal in wild-type axons distal segments increased immediately and subsequently decayed with a near constant slope, whereas fluorescence remained nearly

undetectable in Sarm1-deficient distal axon segments (Figure 5B). Next, we examined the Ca^{2+} levels in mitochondria and the endoplasmic reticulum (ER) using genetically encoded vital sensors, respectively Mito-RGECO (Figure 5C-D) and ER-GCaMP3 (Figure 5E-F). We selected these organelles because Ca^{2+} release from the axonal ER activates the mitochondrial permeability transition pore to trigger axonal degeneration (69, 70). We found elevation of mitochondrial and reticular Ca^{2+} levels after axon severing, but no quantitative difference between severed wild-type and Sarm1-/- animals (Figure 5D,F). These results reveal that loss of Sarm1 attenuates calcium influx to the axoplasm, but not Ca^{2+} uptake in mitochondria or the ER.

Because the second Ca^{2+} wave is responsible for the activation of the serine-threonine protease Calpain, which in turn facilitates axonal fragmentation by cleaving microtubules and neurofilaments (71), we decided to monitor Ca^{2+} levels in lateralis sensory axons 2, 4, 8 and 12 hours-post-injury (hpi). In severed wild-type axons, the second wave of axoplasmic Ca^{2+} starts 4 hpi in coincidence with axon fragmentation, and remains elevated in axonal debris up until 8 hpi (Figure 5G). Note that the temporal resolution of these images does not allow the resolution of degeneration before axonal regeneration. By contrast, the second wave of axoplasmic Ca^{2+} does not occur in Sarm1-mutant axons (Figure 5H). Next, we tested whether enforced elevation of axoplasmic Ca^{2+} is sufficient to trigger the degradation of severed Sarm1-deficient axons. To this end, we transgenically expressed the rat transient receptor potential cation channel subfamily V member 1 (TRPV1) fused to tagRFP in lateralis afferent neurons of Sarm1-mutant zebrafish. Expression of mCherry alone in neurons served

as control. TRPV1 is non-selective cation channel that exhibits a high divalent selectivity, and whose activation produces an influx of Ca^{2+} into cells (72). Rat TRPV1 is activated by temperatures above 43°C or by the vanilloid capsaicin. Importantly, this TRPV1 is inactive at the temperature used to maintain zebrafish (28°C), and zebrafish TRPV1 orthologs are insensitive to capsaicin (73). Therefore, rat TRPV1 expressed in zebrafish offers a tunable tool to elevate axoplasmic Ca^{2+} with excellent temporal resolution. We severed TRPV1-expressing and mCherry-expressing lateralis axons, and 2 hours later a vehicle solution or vehicle + capsaicin were added in the water holding the fish (Figure 5I). Samples were inspected 90 minutes later. Severed Sarm1-deficient axons not expressing TRPV1 did not fragment in presence of capsaicin (Figure 5J), or TRPV1-expressing axons bathed in ethanol solution (Figure 5K). However, Sarm1-deficient TRPV1-expressing axon segments readily degraded in the presence of capsaicin (Figure 5L). Thus, elevation of axoplasmic Ca^{2+} downstream of Sarm1 is sufficient to trigger axon degradation *in vivo*.

Schwann cells are not essential for the maintenance of Sarm1-/- axon segments

The Schwann cells support, fasciculate and myelinate sensory axons in vertebrates (74). They also present phagocytic activity to eliminate damaged axons. We reasoned that delayed axon degeneration by loss of Sarm1 might impact the interaction between axons and Schwann cells. To assess this interaction *in vivo*, we combined the *sarm1*^{hzm13} allele with the triple transgenic line *Tg[gSAGFF202A ; UAS-GFP ; SILL:mCherry]* to highlight the Schwann cells with green fluorescence and the lateralis afferent neurons

with red fluorescence (53, 75). Using high-resolution intravital microscopy, we ascertained that Schwann cells develop normally and fasciculate sensory axons in Sarm1-deficient zebrafish (Figure 6A). Upon severing, wild-type axons were quickly cleared by the Schwann cells through engulfment of axonal fragments and intracellular degradation of debris (Figure 6B). However, there was no axon fragmentation or phagocytic activity by the Schwann cells in Sarm1 mutants (Figure 6B). Next, we asked if Schwann cells are necessary for the maintenance of severed Sarm1-deficient axons by generating a double mutant zebrafish line concurrently deficient for Erbb2, which is generally required in Schwann cells for their migration along the axons, and Sarm1 (76). Loss of Erbb2 in zebrafish leads to the lateralis nerve unmyelination and defasciculation (53, 76). In Erbb2-deficient specimens, the distal portion of the severed axons fragmented and were cleared (Figure 6C) but with a significant delay compared to wild-type specimens (Figure 6D). By contrast, in Erbb2/Sarm1 double mutants, severed axons did not fragment or degrade, identically to fish lacking only Sarm1 (Figure 6C-D). Thus, axon maintenance in Sarm1 mutants occurs independently of the Schwann cells, and that their eventual clearance is performed by other cells.

When an injury generates a gap in the glia, wound-adjacent Schwann cells actively move and extend cellular projections resembling filopodia to quickly reconstitute a continuous glial scaffold (53). Although continuous glia are not necessary for the re-growth of the proximal axon stump, it prevents regenerating growth cones from straying, in turn facilitating end-organ *de novo* innervation and circuit reconstitution (39,

41). Thus, we decided to interrogate Schwann-cell behavior immediately after axon severing and during axon regeneration combining *Tg[gSAGFF202A;UAS-GFP ; SILL:mCherry]* double transgene with the Sarm1 mutation. As expected, we found that in wild-type animals, the Schwann cells adjacent to the wound quickly extended filopodia to close the gap in the glial scaffold ahead of axonal regeneration (Supplemental Movie 1). Re-growing fibers then followed these sub-cellular glial bridges to reconstitute the nerve, suffering mild defasciculation restricted to a small area within the injury (Figure 6E and Supplemental Figure 1). In stark contrast, injury-adjacent Schwann cells did not migrate or produce filopodia-like projections in Sarm1 mutants (Supplemental Movie 2). Nonetheless, regenerating axons eventually negotiated the persistent larger gap to grow along the distal glial scaffold. However, the reforming nerves presented more pronounced local defasciculation (Figure 6F and Supplemental Figure 2).

Schwann-cell do not change phenotype after axon severing in Sarm1-mutant zebrafish

Denervated Schwann cells undergo partial dedifferentiation from myelinating to a progenitor-like state as revealed by loss of expression of terminal-phenotype markers, including myelin and myelin-associated proteins (25, 77, 78). The loss of terminal phenotype promotes Schwann-cell proliferation and migration, which enhances their regenerative function (79). We hypothesized that because Schwann-cell denervation does not occur in Sarm1-mutants, distal Schwann cells may not dedifferentiate. This would explain their lack of phagocytic and protrusive activities after axon transection.

Following this rationale, we immunostained samples with an antibody to Claudin-k, which localizes to the junctions between mature Schwann cells and is downregulated in denervated glia (41, 80). In wild-type specimens, Claudin-k remained strongly expressed along the entire length of the lateralis afferent nerve up to 6 hours after nerve injury (hpi), suggesting that distal Schwann cells remain mature during distal-axon fragmentation (Figure 7A-B). Beginning at 10 hpi, however, distal Schwann cells had markedly less Claudin-k than proximal cells. Finally, 24 hpi Claudin-k was conspicuously absent from distal Schwann cells even after axons regeneration had commenced. By contrast, Claudin-k remained strongly expressed after axon severing in Sarm1-mutant animals during the same period, with no apparent difference between Schwann cells located at either side of the wound (Figure 7A,C). Next, we assessed myelination using the 6D2 monoclonal antibody, which recognizes a carbohydrate epitope in the piscine P0-like myelin glycoproteins IP1 and IP2 (81, 82). As with Claudin-k, 6D2 labeling faded in Schwann cells distal to the injury in wild-type specimens (Figure 7D). Yet, 6D2 labeling remained unchanged in Sarm1 mutants (Figure 7E). We obtained congruent results when addressing myelination directly in living specimens by using a transgenic line expressing membrane-targeted EGFP under the control of the myelin binding protein (Mbp:EGFP-CAAX, green) (Figure 7F-G) (83). Taken together, these results indicate that Sarm1-deficient sensory axons are maintained independently of Schwann-cell support, and that the clearance the severed axons is not necessary for regenerating axon growth, pathfinding, myelination and re-innervation of sensory organs. In addition, they reveal that Schwann cells distal to the injury do not de-differentiate in Sarm1-mutants specimens.

Loss of Sarm1 protects Schwann cells against chemotoxicity

Many chemotherapeutic agents invariably cause peripheral neurotoxicity, leading to permanent neuronal dysfunction (84-88). Previous studies have revealed that under conditions of denervation, Schwann cells become strongly susceptible to chemotoxicity (89, 90). Therefore, we wondered whether the protracted maintenance of severed axons in Sarm1 mutants might counteract glial vulnerability to chemotoxicity. To test this possibility, we treated wild-type and Sarm1-mutant zebrafish with several chemical compounds that are under clinical trials or that are currently used as first-line treatment for common cancers in humans. First, we used 10-Hydroxycamptothecin (10-HCT), which is extremely toxic to denervated glia in zebrafish (91), and counted Schwann cells using the fluorescence transgenic marker *Tg[gSAGFF202A ; UAS:EGFP]*. This marker is ideal for this experiment because the intensity of green fluorescence does not change in denervated Schwann cells and, therefore, it is independent of the maturity of these glia (41). The quantification of Schwann cells confirmed the previous report that 10-HCT does not affects in Schwann cells associated to viable axons (Figure 8A-B) (91). However, we found a significant reduction in the number of Schwann cells in 10-HTC-treated wild-type animals 24 hpi (Figure 8B). Schwann-cell death was more pronounced 48 hpi. By contrast, the number of distal Schwann cells were only marginally affected in Sarm1-mutant specimens 24 hpi, and nearly identical to untreated animals 48 hpi. Platinum-based, taxanes and some alkaloids are effective chemotherapeutic agents used as standards-of-care for various human malignancies, despite their severe neuropathic

effects that include glial destruction (90). To address their effect on Schwann cell, we treated wild-type or Sarm1 mutant zebrafish with cisplatin, oxaliplatin, paclitaxel, docetaxel and vincristine. We found that upon nerve transection, all these drugs invariably killed injury-distal Schwann cells in wild-type specimens but not in Sarm1 mutants (Figure 8C). Importantly, because none of these drugs affected Schwann cells associated with intact axons, we conclude that non-degradable axons non-autonomously protect Schwann cells from chemical stress.

DISCUSSION

The sensory neurons that innervate skin, sensory receptors, joints and muscle communicate peripheral information to the brain, enabling animals to perform the essential activities of daily life. Peripheral and autonomic neuropathies in humans, derived from chemical stress, chronic metabolic disease, or physical damage from head concussions, motor-vehicle and sporting accidents are common cause of neural injury, leading to axon degeneration. The consequent nerve loss often has significant negatively impact on the quality of life of the affected individuals. Using zebrafish and a battery of tests that include subcellular structural characterization of sensory neurons and associated Schwann cells, neuronal-function, and behavioral assays, we offer a comprehensive and integrated analysis of neuronal and glial response to injury, as well as on the consequences of blocking axon degeneration systemically.

In vertebrates, severed axons invariably degenerate rapidly. We wondered about the benefit of fast axonal degradation to the organism, in particular because some

invertebrates that include crayfish, roundworms and leeches maintain injured axons with no signs of degeneration (92, 93). For instance, the roundworm *C. elegans* maintains severed axons despite these animals bearing a TIR-1/Sarm1 protein with conserved pro-degenerative activity. Strikingly, transected axon segments in *C. elegans* reseal to rapidly reconstitute the neuronal circuit (64). This appears to be a very effective strategy to recover neural function with high fidelity. Yet, axon resealing has not been observed in other species, begging the question of why vertebrates do not use a similar mechanism after nerve injury. One possibility is that the degradation of severed axons is too fast to enable resealing. Alternatively, resealing events may have remained hidden owing to the technical difficulties associated to imaging axonal behavior in living vertebrates. Taking advantage of zebrafish lacking Sarm1 and its amenability for high-resolution intravital imaging, we tested whether the protracted maintenance of severed axons allows axon-segment resealing. We devised a strategy that employs fluorescent-protein photoconversion to unambiguously mark individual sensory neurons and identify proximal and distal axon segments after transection and during regeneration. Yet, we could never see any fusion event between axons segments. Instead, regenerating axons grew past the non-degradable distal segments to re-innervate peripheral synaptic targets. Whether other neuronal classes undergo axon-segment fusion remains to be tested. Yet, we can conclude that axon resealing is not a general feature of the vertebrate nervous system. Moreover, using multiparametric tests in Sarm1 mutants, we demonstrate that the long-term maintenance of non-degradable axon fragments has no detrimental effect on the repair of a sensory circuit. We also found that sensorimotor recovery after nerve repair

is not contingent upon speedy clearance of severed axons, revealing that the axonal destructive and nerve reconstructive processes occur in parallel. Furthermore, regenerating axons fasciculate and re-myelinate normally, indicating that they do not compete with non-degradable axons segments for exiting glia. Therefore, a competitive balance between axon degradation and regeneration does not appear to have shaped the evolution of Sarm1 and, by extension, Wallerian degeneration.

Focusing on Schwann cells, we show that glial cells adjacent to nerve injury in Sarm1 mutants behave dramatically different than those of wild-type specimens. Specifically, Schwann cells in Sarm1 mutants do not migrate or extend projections to bridge the gap in the glial scaffold, indicating that these cells do not directly sense missing intercellular contacts or glial discontinuity. Instead, our findings suggest alternative scenarios. One is that the degradation of axons releases signals that induce Schwann cell to change behavior. In mice, for example, nerve damage promotes mesenchymal behavior of Schwann cells surrounding the wound via TGF-β signaling, which drives collective Schwann-cell migration across the wound (94). Although we did not observe Schwann-cell migration, signals derived from injured axons may promote wound-adjacent Schwann cells to extend projections to bridge the gap in a similar manner. Interestingly, we observed that filopodia-like structures emerged from Schwann cells at both sides of the injury in wild-type animals, suggesting that repair-inducing signals are likely diffusible, affecting glial cells independently of their association with axons. It remains to be determined if the source of such signals is the degrading axons, the denervated Schwann cells, or other cells that are recruited to the wound.

Loss of Sarm1 improves functional recovery after traumatic brain injury, as well as vincristine-mediated neurotoxicity in mice (95, 96). Yet, the therapeutic potential of blocking axon degeneration systemically remains uncertain. We found that chronic and systemic loss of Sarm1 is compatible with zebrafish viability and sensorineural function. Similarly, Sarm1-deficient mice are viable (19, 97). Interestingly, data from the Genetic Testing Registry reveal that Sarm1 variants in humans have so far only been associated to congenital defect of folate absorption (*https://www.ncbi.nlm.nih.gov/gtr/all/tests/?term=607732[mim]*) (98). Nevertheless, dietary reduction of folates can prevent the appearance of symptoms of folate absorption defect (99). Therefore, in zebrafish, mouse and humans, Sarm1 appears to be a non-essential protein whose deficit is associated to mild conditions. As a discrete hierarchical factor that is essential for axon degeneration, Sarm1 is an ideal target for pharmacological interventions (18). The generality of this conclusion gains persuasiveness by a comprehensive examination of genomic data of over 60.000 humans from the Exome Aggregation Consortium (ExAC) database, which revealed many healthy individuals carrying biallelic missense, frameshift and splice-site mutations in Sarm1 (*http://exac.broadinstitute.org/gene/ENSG00000004139*) (100).

CONCLUSION

Enhancing stress tolerance is a promising strategy to protect vulnerable cells from harsh conditions. The impact on the organim of inhibiting Sarm1 is difficult to predict because so far no exhaustive study of systemic supression of Wallerian axon

degeneration has been done. We have exploited a simple *in vivo* genetic system to comprehensively study the consequence of mutations in Sarm1. We demonstrate that the the loss os Sarm1 is well tolerated by the animal, and that the protracted maintenance of transected axons increases Schwann-cell tolerance to toxicity by diverse chemotherapeutic agents. Importantly, these data lend strong support to the idea that direct interventions to systemically inhibit axon degradation are promising strategies to reduce chronic consequences of neurotrauma. Because TIR domain dimerization is necessary and sufficient to degrade NAD+, it renders Sarm1 amenable to inhibition by small molecules, as it has been demosntrated for the TIR domain of TLR2 (106). Thus, our findings encourage the development of Sarm1 inhibitors for therapeutic applications (18, 29).

REFERENCES

1. Ameh V, and Crane S. Nerve injury following shoulder dislocation: the emergency physician's perspective. *Eur J Emerg Med.* 2006;13(4):233-5.
2. Heneka MT, Carson MJ, El Khoury J, Landreth GE, Brosseron F, Feinstein DL, Jacobs AH, Wyss-Coray T, Vitorica J, Ransohoff RM, et al. Neuroinflammation in Alzheimer's disease. *Lancet Neurol.* 2015;14(4):388-405.
3. Missios S, Bekelis K, and Spinner RJ. Traumatic peripheral nerve injuries in children: epidemiology and socioeconomics. *J Neurosurg Pediatr.* 2014;14:688-94.
4. Rowe RK, Ellis GI, Harrison JL, Bachstetter AD, Corder GF, Van Eldik LJ, Taylor BK, Marti F, and Lifshitz J. Diffuse traumatic brain injury induces prolonged immune dysregulation and potentiates hyperalgesia following a peripheral immune challenge. *Mol Pain.* 2016;12(
5. Tzekov R, Phifer J, Myers A, Mouzon B, and Crawford F. Inflammatory changes in optic nerve after closed-head repeated traumatic brain injury: Preliminary study. *Brain Inj.* 2016;30(12):1428-35.
6. Ziogas NK, and Koliatsos VE. Primary Traumatic Axonopathy in Mice Subjected to Impact Acceleration: A Reappraisal of Pathology and Mechanisms with High-Resolution Anatomical Methods. *J Neurosci.* 2018;38(16):4031-47.

7. Roselli F, and Caroni P. From intrinsic firing properties to selective neuronal vulnerability in neurodegenerative diseases. *Neuron.* 2015;85(5):901-10.
8. Cattin AL, and Lloyd AC. The multicellular complexity of peripheral nerve regeneration. *Curr Opin Neurobiol.* 2016;39(38-46.
9. Parrinello S, Napoli I, Ribeiro S, Wingfield Digby P, Fedorova M, Parkinson DB, Doddrell RD, Nakayama M, Adams RH, and Lloyd AC. EphB signaling directs peripheral nerve regeneration through Sox2-dependent Schwann cell sorting. *Cell.* 2010;143(1):145-55.
10. Ziegenfuss JS, Doherty J, and Freeman MR. Distinct molecular pathways mediate glial activation and engulfment of axonal debris after axotomy. *Nat Neurosci.* 2012;15(7):979-87.
11. Harrisingh MC, Perez-Nadales E, Parkinson DB, Malcolm DS, Mudge AW, and Lloyd AC. The Ras/Raf/ERK signalling pathway drives Schwann cell dedifferentiation. *EMBO J.* 2004;23(15):3061-71.
12. Scherer SS. The biology and pathobiology of Schwann cells. *Curr Opin Neurol.* 1997;10(5):386-97.
13. Waller A. Experiments on the Section of the Glossopharyngeal and Hypoglossal Nerves of the Frog, and Observations of the Alterations Produced Thereby in the Structure of Their Primitive Fibres. *Philosophical Transactions of the Royal Society of London.*140(423-9
14. Gerdts J, Summers DW, Milbrandt J, and DiAntonio A. Axon Self-Destruction: New Links among SARM1, MAPKs, and NAD+ Metabolism. *Neuron.* 2016;89(3):449-60.
15. Osterloh JM, Yang J, Rooney TM, Fox AN, Adalbert R, Powell EH, Sheehan AE, Avery MA, Hackett R, Logan MA, et al. dSarm/Sarm1 is required for activation of an injury-induced axon death pathway. *Science.* 2012;337(6093):481-4.
16. Walker LJ, Summers DW, Sasaki Y, Brace EJ, Milbrandt J, and DiAntonio A. MAPK signaling promotes axonal degeneration by speeding the turnover of the axonal maintenance factor NMNAT2. *Elife.* 2017;6(
17. Yang J, Wu Z, Renier N, Simon DJ, Uryu K, Park DS, Greer PA, Tournier C, Davis RJ, and Tessier-Lavigne M. Pathological axonal death through a MAPK cascade that triggers a local energy deficit. *Cell.* 2015;160(1-2):161-76.
18. Essuman K, Summers DW, Sasaki Y, Mao X, DiAntonio A, and Milbrandt J. The SARM1 Toll/Interleukin-1 Receptor Domain Possesses Intrinsic NAD(+) Cleavage Activity that Promotes Pathological Axonal Degeneration. *Neuron.* 2017;93(6):1334-43 e5.
19. Gerdts J, Summers DW, Sasaki Y, DiAntonio A, and Milbrandt J. Sarm1-mediated axon degeneration requires both SAM and TIR interactions. *J Neurosci.* 2013;33(33):13569-80.
20. Gerdts J, Brace EJ, Sasaki Y, DiAntonio A, and Milbrandt J. SARM1 activation triggers axon degeneration locally via NAD(+) destruction. *Science.* 2015;348(6233):453-7.

21. Loreto A, Di Stefano M, Gering M, and Conforti L. Wallerian Degeneration Is Executed by an NMN-SARM1-Dependent Late Ca(2+) Influx but Only Modestly Influenced by Mitochondria. *Cell Rep.* 2015;13(11):2539-52.
22. Summers DW, Gibson DA, DiAntonio A, and Milbrandt J. SARM1-specific motifs in the TIR domain enable NAD+ loss and regulate injury-induced SARM1 activation. *Proc Natl Acad Sci U S A.* 2016;113(41):E6271-E80.
23. Essuman K, Summers DW, Sasaki Y, Mao X, Yim AKY, DiAntonio A, and Milbrandt J. TIR Domain Proteins Are an Ancient Family of NAD(+)-Consuming Enzymes. *Curr Biol.* 2018;28(3):421-30 e4.
24. Sasaki Y, Nakagawa T, Mao X, DiAntonio A, and Milbrandt J. NMNAT1 inhibits axon degeneration via blockade of SARM1-mediated NAD(+) depletion. *Elife.* 2016;5(
25. Jessen KR, Mirsky R, and Lloyd AC. Schwann Cells: Development and Role in Nerve Repair. *Cold Spring Harb Perspect Biol.* 2015;7(7):a020487.
26. Jortner BS. Mechanisms of toxic injury in the peripheral nervous system: neuropathologic considerations. *Toxicol Pathol.* 2000;28(1):54-69.
27. Morell P, and Toews AD. Schwann cells as targets for neurotoxicants. *Neurotoxicology.* 1996;17(3-4):685-95.
28. Koeppen AH. Wallerian degeneration: history and clinical significance. *J Neurol Sci.* 2004;220(1-2):115-7.
29. Simon DJ, and Watkins TA. Therapeutic opportunities and pitfalls in the treatment of axon degeneration. *Curr Opin Neurol.* 2018;31(6):693-701.
30. Schuldiner O, and Yaron A. Mechanisms of developmental neurite pruning. *Cell Mol Life Sci.* 2015;72(1):101-19.
31. Omura T, Omura K, Tedeschi A, Riva P, Painter MW, Rojas L, Martin J, Lisi V, Huebner EA, Latremoliere A, et al. Robust Axonal Regeneration Occurs in the Injured CAST/Ei Mouse CNS. *Neuron.* 2015;86(5):1215-27.
32. D'Rozario M, Monk KR, and Petersen SC. Analysis of myelinated axon formation in zebrafish. *Methods Cell Biol.* 2017;138(383-414.
33. Friedrich RW, Genoud C, and Wanner AA. Analyzing the structure and function of neuronal circuits in zebrafish. *Front Neural Circuits.* 2013;7(71.
34. Friedrich RW, Jacobson GA, and Zhu P. Circuit neuroscience in zebrafish. *Curr. Biol.* 2010;20(8):R371-81.
35. Ackerman SD, Garcia C, Piao X, Gutmann DH, and Monk KR. The adhesion GPCR Gpr56 regulates oligodendrocyte development via interactions with Galpha12/13 and RhoA. *Nat Commun.* 2015;6(6122.
36. Bin JM, and Lyons DA. Imaging Myelination In Vivo Using Transparent Animal Models. *Brain Plast.* 2016;2(1):3-29.
37. Fontenas L, and Kucenas S. Livin' On The Edge: glia shape nervous system transition zones. *Curr Opin Neurobiol.* 2017;47(44-51.
38. Ohki Y, Wenninger-Weinzierl A, Hruscha A, Asakawa K, Kawakami K, Haass C, Edbauer D, and Schmid B. Glycine-alanine dipeptide repeat protein contributes to toxicity in a zebrafish model of C9orf72 associated neurodegeneration. *Mol Neurodegener.* 2017;12(1):6.

39. Rosenberg AF, Isaacman-Beck J, Franzini-Armstrong C, and Granato M. Schwann cells and deleted in colorectal carcinoma direct regenerating motor axons towards their original path. *J Neurosci.* 2014;34(44):14668-81.
40. Wehner D, Tsarouchas TM, Michael A, Haase C, Weidinger G, Reimer MM, Becker T, and Becker CG. Wnt signaling controls pro-regenerative Collagen XII in functional spinal cord regeneration in zebrafish. *Nat Commun.* 2017;8(1):126.
41. Xiao Y, Faucherre A, Pola-Morell L, Heddleston JM, Liu TL, Chew TL, Sato F, Sehara-Fujisawa A, Kawakami K, and López-Schier H. High-resolution live imaging reveals axon-glia interactions during peripheral nerve injury and repair in zebrafish. *Dis Model Mech.* 2015;8(6):553-64.
42. O'Donnell KC, Vargas ME, and Sagasti A. WldS and PGC-1alpha regulate mitochondrial transport and oxidation state after axonal injury. *J Neurosci.* 2013;33(37):14778-90.
43. Conforti L, Gilley J, and Coleman MP. Wallerian degeneration: an emerging axon death pathway linking injury and disease. *Nat Rev Neurosci.* 2014;15(6):394-409.
44. Howe K, Clark MD, Torroja CF, Torrance J, Berthelot C, Muffato M, Collins JE, Humphray S, McLaren K, Matthews L, et al. The zebrafish reference genome sequence and its relationship to the human genome. *Nature.* 2013;496(7446):498-503.
45. Sztal TE, Ruparelia AA, Williams C, and Bryson-Richardson RJ. Using Touch-evoked Response and Locomotion Assays to Assess Muscle Performance and Function in Zebrafish. *J Vis Exp.* 2016116).
46. Ghysen A, and Dambly-Chaudiere C. The lateral line microcosmos. *Genes Dev.* 2007;21(17):2118-30.
47. Pujol-Martí J, and López-Schier H. Developmental and architectural principles of the lateral-line neural map. *Front Neural Circuits.* 2013;7(47.
48. Drerup CM, and Nechiporuk AV. In vivo analysis of axonal transport in zebrafish. *Methods Cell Biol.* 2016;131(311-29.
49. Haehnel-Taguchi M, Akanyeti O, and Liao JC. Behavior, Electrophysiology, and Robotics Experiments to Study Lateral Line Sensing in Fishes. *Integr Comp Biol.* 2018;58(5):874-83.
50. Pujol-Martí J, Faucherre A, Aziz-Bose R, Asgharsharghi A, Colombelli J, Trapani JG, and López-Schier H. Converging axons collectively initiate and maintain synaptic selectivity in a constantly remodeling sensory organ. *Curr Biol.* 2014;24(24):2968-74.
51. Olt J, Ordoobadi AJ, Marcotti W, and Trapani JG. Physiological recordings from the zebrafish lateral line. *Methods Cell Biol.* 2016;133(253-79.
52. Vargas ME, Yamagishi Y, Tessier-Lavigne M, and Sagasti A. Live Imaging of Calcium Dynamics during Axon Degeneration Reveals Two Functionally Distinct Phases of Calcium Influx. *J Neurosci.* 2015;35(45):15026-38.
53. Xiao Y, Tian W, and López-Schier H. Optogenetic stimulation of neuronal repair. *Curr Biol.* 2015;25(22):R1068-9.

54. Haehnel-Taguchi M, Akanyeti O, and Liao JC. Afferent and motoneuron activity in response to single neuromast stimulation in the posterior lateral line of larval zebrafish. *J Neurophysiol.* 2014;112(6):1329-39.
55. Olive R, Wolf S, Dubreuil A, Bormuth V, Debregeas G, and Candelier R. Rheotaxis of Larval Zebrafish: Behavioral Study of a Multi-Sensory Process. *Front Syst Neurosci.* 2016;10(14.
56. Oteíza P, Odstrcil I, Lauder G, Portugues R, and Engert F. A novel mechanism for mechanosensory-based rheotaxis in larval zebrafish. *Nature.* 2017;547(7664):445-8.
57. Kim MJ, Kang KH, Kim CH, and Choi SY. Real-time imaging of mitochondria in transgenic zebrafish expressing mitochondrially targeted GFP. *Biotechniques.* 2008;45(3):331-4.
58. Mandal A, Pinter K, and Drerup CM. Analyzing Neuronal Mitochondria in vivo Using Fluorescent Reporters in Zebrafish. *Front Cell Dev Biol.* 2018;6(144.
59. Lin MY, Cheng XT, Tammineni P, Xie Y, Zhou B, Cai Q, and Sheng ZH. Releasing Syntaphilin Removes Stressed Mitochondria from Axons Independent of Mitophagy under Pathophysiological Conditions. *Neuron.* 2017;94(3):595-610 e6.
60. Miller KE, and Sheetz MP. Axonal mitochondrial transport and potential are correlated. *J Cell Sci.* 2004;117(Pt 13):2791-804.
61. Liao JC, and Haehnel M. Physiology of afferent neurons in larval zebrafish provides a functional framework for lateral line somatotopy. *J Neurophysiol.* 2012;107(10):2615-23.
62. Gilley J, Ribchester RR, and Coleman MP. Sarm1 Deletion, but Not Wld(S), Confers Lifelong Rescue in a Mouse Model of Severe Axonopathy. *Cell Rep.* 2017;21(1):10-6.
63. Xiao Y, and López-Schier H. Studying Axonal Regeneration by Laser Microsurgery and High-Resolution Videomicroscopy. *Methods Mol Biol.* 2016;1451(271-80.
64. Neumann B, Coakley S, Giordano-Santini R, Linton C, Lee ES, Nakagawa A, Xue D, and Hilliard MA. EFF-1-mediated regenerative axonal fusion requires components of the apoptotic pathway. *Nature.* 2015;517(7533):219-22.
65. Neumann B, Nguyen KC, Hall DH, Ben-Yakar A, and Hilliard MA. Axonal regeneration proceeds through specific axonal fusion in transected C. elegans neurons. *Dev Dyn.* 2011;240(6):1365-72.
66. Ando R, Hama H, Yamamoto-Hino M, Mizuno H, and Miyawaki A. An optical marker based on the UV-induced green-to-red photoconversion of a fluorescent protein. *Proc Natl Acad Sci U S A.* 2002;99(20):12651-6.
67. Ozaki T, Yamashita T, and Ishiguro S. Mitochondrial m-calpain plays a role in the release of truncated apoptosis-inducing factor from the mitochondria. *Biochim Biophys Acta.* 2009;1793(12):1848-59.
68. Muto A, Ohkura M, Abe G, Nakai J, and Kawakami K. Real-time visualization of neuronal activity during perception. *Curr. Biol.* 2013;23:307-11.
69. Court FA, and Coleman MP. Mitochondria as a central sensor for axonal degenerative stimuli. *Trends Neurosci.* 2012;35(6):364-72.

70. Villegas R, Martínez NW, Lillo J, Pihan P, Hernández D, Twiss JL, and Court FA. Calcium release from intra-axonal endoplasmic reticulum leads to axon degeneration through mitochondrial dysfunction. *J. Neurosci.* 2014;34:7179-89.
71. Park JY, Jang SY, Shin YK, Suh DJ, and Park HT. Calcium-dependent proteasome activation is required for axonal neurofilament degradation. *Neural Regen Res.* 2013;8(36):3401-9.
72. Caterina MJ, Schumacher MA, Tominaga M, Rosen TA, Levine JD, and Julius D. The capsaicin receptor: a heat-activated ion channel in the pain pathway. *Nature.* 1997;389(6653):816-24.
73. Gau P, Poon J, Ufret-Vincenty C, Snelson CD, Gordon SE, Raible DW, and Dhaka A. The zebrafish ortholog of TRPV1 is required for heat-induced locomotion. *J Neurosci.* 2013;33(12):5249-60.
74. Brosius Lutz A, and Barres BA. Contrasting the glial response to axon injury in the central and peripheral nervous systems. *Dev Cell.* 2014;28(1):7-17.
75. Faucherre A, Pujol-Martí J, Kawakami K, and López-Schier H. Afferent neurons of the zebrafish lateral line are strict selectors of hair-cell orientation. *PLoS One.* 2009;4(2):e4477.
76. Lyons DA, Pogoda HM, Voas MG, Woods IG, Diamond B, Nix R, Arana N, Jacobs J, and Talbot WS. erbb3 and erbb2 are essential for schwann cell migration and myelination in zebrafish. *Curr Biol.* 2005;15(6):513-24.
77. Sasaki Y, Hackett AR, Kim S, Strickland A, and Milbrandt J. Dysregulation of NAD(+) Metabolism Induces a Schwann Cell Dedifferentiation Program. *J Neurosci.* 2018;38(29):6546-62.
78. Soto J, and Monje PV. Axon contact-driven Schwann cell dedifferentiation. *Glia.* 2017;65(6):864-82.
79. Carr MJ, and Johnston AP. Schwann cells as drivers of tissue repair and regeneration. *Curr Opin Neurobiol.* 2017;47(52-7.
80. Munzel EJ, Schaefer K, Obirei B, Kremmer E, Burton EA, Kuscha V, Becker CG, Brosamle C, Williams A, and Becker T. Claudin k is specifically expressed in cells that form myelin during development of the nervous system and regeneration of the optic nerve in adult zebrafish. *Glia.* 2012;60(2):253-70.
81. López-Schier H, and Hudspeth AJ. Supernumerary neuromasts in the posterior lateral line of zebrafish lacking peripheral glia. *Proc Natl Acad Sci U S A.* 2005;102(5):1496-501.
82. Bastmeyer M, Jeserich G, and Stuermer CA. Similarities and differences between fish oligodendrocytes and Schwann cells in vitro. *Glia.* 1994;11:300-14.
83. Czopka T, Ffrench-Constant C, and Lyons DA. Individual oligodendrocytes have only a few hours in which to generate new myelin sheaths in vivo. *Dev Cell.* 2013;25(6):599-609.
84. Cavaletti G, Alberti P, and Marmiroli P. Chemotherapy-induced peripheral neurotoxicity in the era of pharmacogenomics. *Lancet Oncol.* 2011;12:1151-61.
85. Kaiser J, Bledowski C, and Dietrich J. Neural correlates of chemotherapy-related cognitive impairment. *Cortex.* 2014;54(33-50.
86. McLeary F, Davis A, Rudrawar S, Perkins A, and Anoopkumar-Dukie S. Mechanisms underlying select chemotherapeutic-agent-induced

neuroinflammation and subsequent neurodegeneration. *Eur J Pharmacol.* 2018;842(49-56.

87. Fukuda Y, Li Y, and Segal RA. A Mechanistic Understanding of Axon Degeneration in Chemotherapy-Induced Peripheral Neuropathy. *Front Neurosci.* 2017;11(481.
88. Gornstein E, and Schwarz TL. The paradox of paclitaxel neurotoxicity: Mechanisms and unanswered questions. *Neuropharmacology.* 2014;76 Pt A(175-83.
89. Diezi M, Buclin T, and Kuntzer T. Toxic and drug-induced peripheral neuropathies: updates on causes, mechanisms and management. *Curr Opin Neurol.* 2013;26(5):481-8.
90. Imai S, Koyanagi M, Azimi Z, Nakazato Y, Matsumoto M, Ogihara T, Yonezawa A, Omura T, Nakagawa S, Wakatsuki S, et al. Taxanes and platinum derivatives impair Schwann cells via distinct mechanisms. *Sci Rep.* 2017;7(1):5947.
91. Bremer J, Skinner J, and Granato M. A small molecule screen identifies in vivo modulators of peripheral nerve regeneration in zebrafish. *PLoS One.* 2017;12(6):e0178854.
92. Frank E, Jansen JK, and Rinvik E. A multisomatic axon in the central nervous system of the leech. *J Comp Neurol.* 1975;159(1):1-13.
93. Hoy RR, Bittner GD, and Kennedy D. Regeneration in crustacean motoneurons: evidence for axonal fusion. *Science.* 1967;156(3772):251-2.
94. Clements MP, Byrne E, Camarillo Guerrero LF, Cattin AL, Zakka L, Ashraf A, Burden JJ, Khadayate S, Lloyd AC, Marguerat S, et al. The Wound Microenvironment Reprograms Schwann Cells to Invasive Mesenchymal-like Cells to Drive Peripheral Nerve Regeneration. *Neuron.* 2017;96(1):98-114 e7.
95. Henninger N, Bouley J, Sikoglu EM, An J, Moore CM, King JA, Bowser R, Freeman MR, and Brown RH, Jr. Attenuated traumatic axonal injury and improved functional outcome after traumatic brain injury in mice lacking Sarm1. *Brain.* 2016;139(Pt 4):1094-105.
96. Geisler S, Doan RA, Strickland A, Huang X, Milbrandt J, and DiAntonio A. Prevention of vincristine-induced peripheral neuropathy by genetic deletion of SARM1 in mice. *Brain.* 2016;139(Pt 12):3092-108.
97. Turkiew E, Falconer D, Reed N, and Hoke A. Deletion of Sarm1 gene is neuroprotective in two models of peripheral neuropathy. *J Peripher Nerv Syst.* 2017;22(3):162-71.
98. Rubinstein WS, Maglott DR, Lee JM, Kattman BL, Malheiro AJ, Ovetsky M, Hem V, Gorelenkov V, Song G, Wallin C, et al. The NIH genetic testing registry: a new, centralized database of genetic tests to enable access to comprehensive information and improve transparency. *Nucleic Acids Res.* 2013;41:D925-35.
99. Czeizel AE, Dudas I, Vereczkey A, and Banhidy F. Folate deficiency and folic acid supplementation: the prevention of neural-tube defects and congenital heart defects. *Nutrients.* 2013;5(11):4760-75.

100. Lek M, Karczewski KJ, Minikel EV, Samocha KE, Banks E, Fennell T, O'Donnell-Luria AH, Ware JS, Hill AJ, Cummings BB, et al. Analysis of protein-coding genetic variation in 60,706 humans. *Nature.* 2016; 536:285-91.
101. Auer F, Vagionitis S, and Czopka T. Evidence for Myelin Sheath Remodeling in the CNS Revealed by In Vivo Imaging. *Curr Biol.* 2018;28(4):549-59 e3.
102. Hwang WY, Fu Y, Reyon D, Maeder ML, Tsai SQ, Sander JD, Peterson RT, Yeh JJ, and Joung JK. Efficient genome editing in zebrafish using a CRISPR-Cas system. *Nature biotechnology.* 2013;31(3):227.
103. Wright DA, Thibodeau-Beganny S, Sander JD, Winfrey RJ, Hirsh AS, Eichtinger M, Fu F, Porteus MH, Dobbs D, Voytas DF, et al. Standardized reagents and protocols for engineering zinc finger nucleases by modular assembly. *Nat Protoc.* 2006;1(3):1637-52.
104. Czopka T, and Lyons DA. Individual oligodendrocytes have only a few hours in which to generate new myelin sheaths in vivo. *Dev. Cell.* 2013;25(6):599-609.
105. Esterberg R, Linbo T, Pickett SB, Wu P, Ou HC, Rubel EW, and Raible DW. Mitochondrial calcium uptake underlies ROS generation during aminoglycoside-induced hair cell death. *J. Clin. Invest.* 2016;126(9):3556-66.
106. Mistry P, Laird MH, Schwarz RS, Greene S, Dyson T, Snyder GA, Xiao TS, Chauhan J, Fletcher S, Toshchakov VY, MacKerell AD Jr, Vogel SN. Inhibition of TLR2 signaling by small molecule inhibitors targeting a pocket within the TLR2 TIR domain. *Proc. Natl. Acad. Sci. U.S.A.* 2015; 112:5455-60.

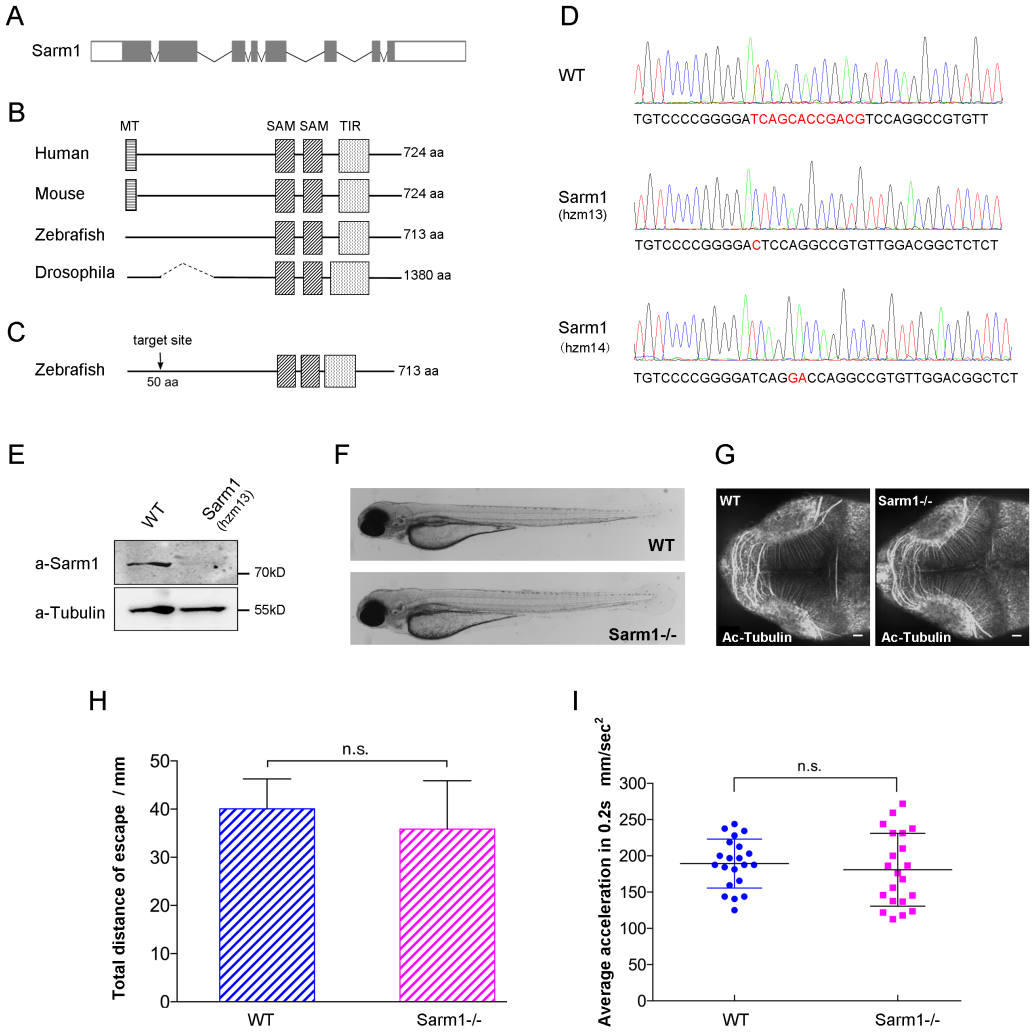

Figure 1. A) Genomic structure of *Danio rerio* Sarm1, indicating the 8 exons, with proteins coding-regions in grey, non-coding region in white, and introns as bent lines (not at scale). **B)** Alignment of the Sarm1 functional domains from different species. **C)** Structure of the zebrafish Sarm1 protein highlighting the two SAM domains (dark grey), the TIR domain (light grey). The downward arrow indicated the approximate region targeted for mutagenesis, approximately 50 amino acids from the start codon. **D)** Sequence of the wild-type Sarm1 indicating in red the mutagenized area and, below, the two mutant alleles obtained in this study. The *hzm13* allele introduces an 11-base deletion and T/C mutation, resulting in a frame shift and premature stop codon. The *hzm14* allele is a 7-base deletion and AG/GA mutation that also generates a frame shift and premature stop codon. **E)** Western blot of protein extracts from wild

type and Sarm1^{hzm13} fish embryos using a commercial ant-Sarm1 antibody, revealing absence of the protein in the mutants. An antibody to alpha-Tubulin was used as loading control. **F)** Low-magnification image of a wild-type 5dpf zebrafish (top) and a homozygous Sarm1^{hzm13} (bottom), showing no overall anatomical differences. **G)** Confocal image of a wild-type 5dpf zebrafish (left) and a homozygous Sarm1^{hzm13} (right) stained with an antibody to acetylated Tubulin to mark neurons in the central nervous system, showing no evident defects in the mutants. In this and all figures, rostral is left and caudal is right. Scale bar 20μm. **H-I)** Quantification of sensorimotor function in zebrafish. (H) shows the total distance traveled by larvae after touch-trigger escape response in wild-type (dashed blue bar) and homozygous Sarm1^{hzm13} (dashed magenta bar). (I) dot plot of the average acceleration of wild-type (blue) and homozygous Sarm1^{hzm13} (magenta) after tactile touch-induced escape response. Error bar = SEM; n.s. means no significant difference, one-way ANOVA. wild type n=21, Sarm1-/- n=21.

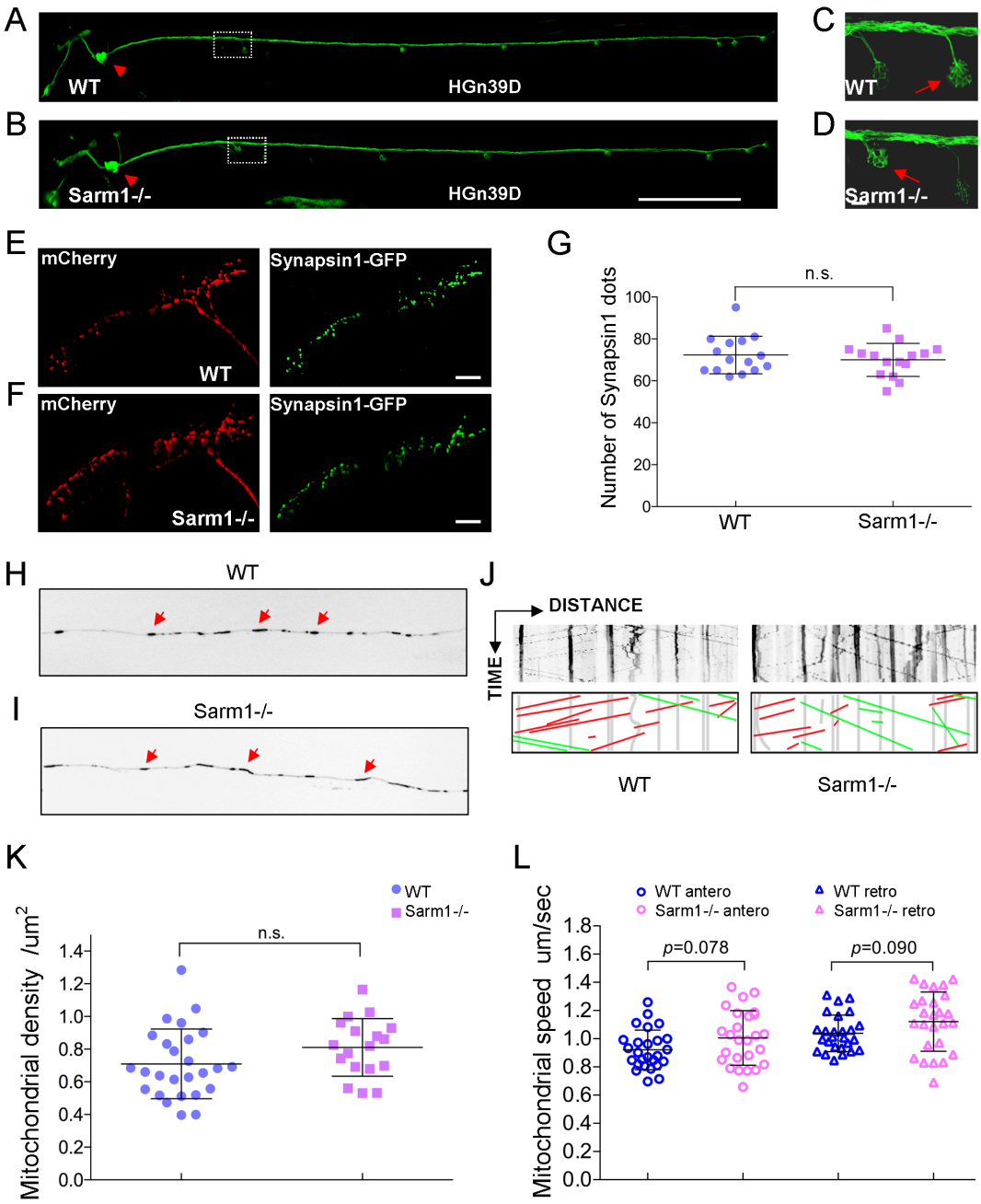

Figure 2. A-B) Confocal image of a 5dpf wild-type (A) and Sarm1-/- (B) larvae carrying the *Tg[HGn39D]* transgene to mark lateralis afferent neurons with GFP. The posterior lateral-line ganglion is indicated with a red arrowhead. The dotted box indicates an innervated neuromast (expanded in C). Scale bar 400**µ**m. **C-D)** Confocal image of the peripheral arborization of lateralis neurons in 5dpf wild-type (C) and Sarm1-/- (D). Red arrows indicate the position of a neuromast from the dotted boxes

in (A-B). **E-F)** Confocal image of the central arborization of lateralis neurons in 5dpf wild-type (E) and Sarm1-/- (F), mCherry (red) and Synapsin1-GFP (green) to reveal normal arborization and pre-synaptic puncta in both cases. **G)** Quantification of the number of synapsin1 puncta from (E-F), Error bar = SEM; n.s. = not significant, one-way ANOVA. Wild type n=15, Sarm1-/- n=15. **H-I)** Confocal image of axonal mitochondria marked with mito-mCherry in wild-type (H) and Sarm1-/- (I). Red arrows point to prominent mitochondrial groups in axons. **J)** Upper panels, kymographs from videomicroscopic recording of axonal mitochondria in wild type (H) (left panel) and Sarm1-/- (I) (right panel). Lower panels show color-coded traces of moving mitochondria in anterograde (green) and retrograde (red) directions, taken from the kymographs shown in the upper panels. **K)** Density of mitochondria in 5dpf wild type and Sarm1-/-, Error bar = SEM; n.s. = not significant, n=25 (WT), n=19 (Sarm1-/-). **L)** Mobility of the mitochondria in 5dpf wild type and Sarm1-/-. Circles show the anterograde and triangles the retrograde movement of the mitochondria. p value from one-way ANOVA, wild type n=26, Sarm1-/- n=26.

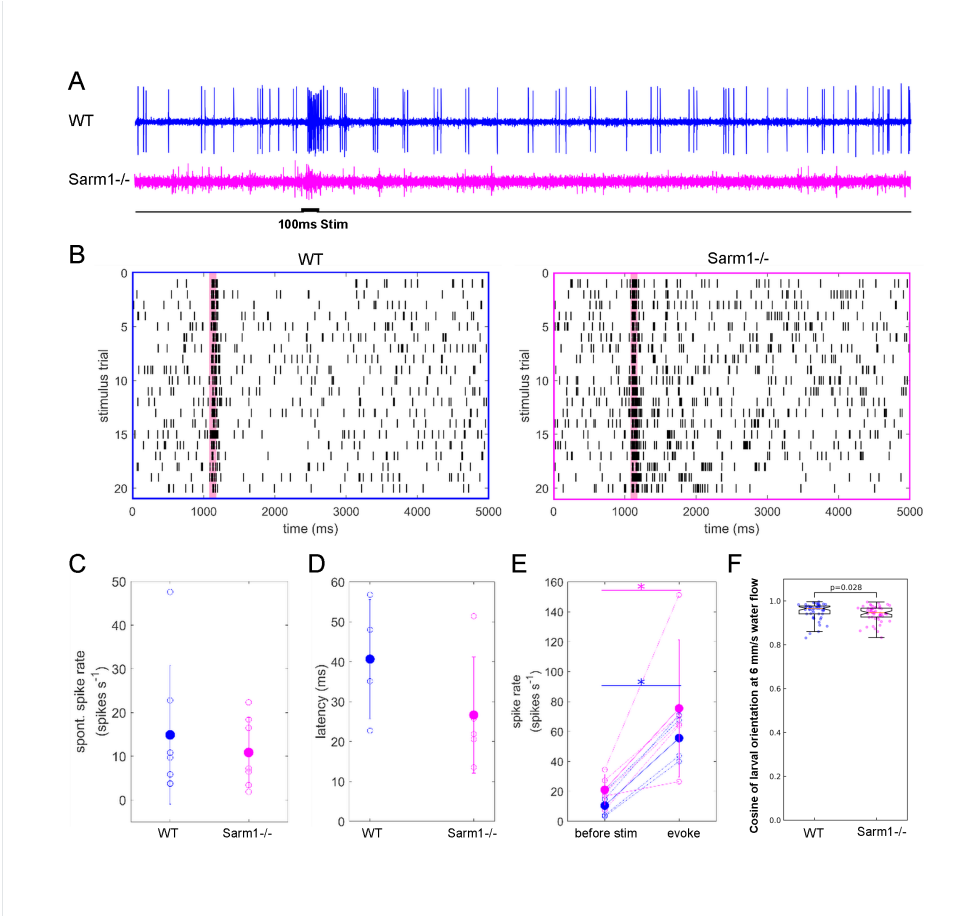

Figure 3. A) Examples of five second long loose patch recordings of mutant and control larva. Stimulus (water jet): 100 ms. Wild type (blue) Sarm1 mutants (magenta). **B)** Raster plots of responses to 20 stimulus repetitions in wild type (blue) and Sarm1-mutant larvae (magenta). **C)** Quantification of spontaneous spike rates from all recorded neurons, averaged over entire recording (12 seconds to 2 minutes). Wild type and Sarm1 mutants show no significant differences (wild type n=7, Sarm1-/- n=7). **D)** Quantification of response latencies of wild type and mutant larvae shows no significant difference (wild type n=4, Sarm1-/- n=5). **E)** Wild type and Sarm1 mutants respond with a significant increase in spike rate to water jet stimulation ($p<0.05$). No significant difference in spike rate was detected between wild type and Sarm1-/- before or after stimulus onset. **F)** Rheotaxis (oriented swimming against water-flow direction) shown as cosine of the orientation of the wild-type and Sarm1-/- larva in 6mm/s water flow, showing a marginal difference between wild-type and Sarm1 mutants. * indicates $p<0.05$, Wilcoxon rank sum test. Wild type n=7 Sarm1-/- n=7. 10 trails for each larvae.

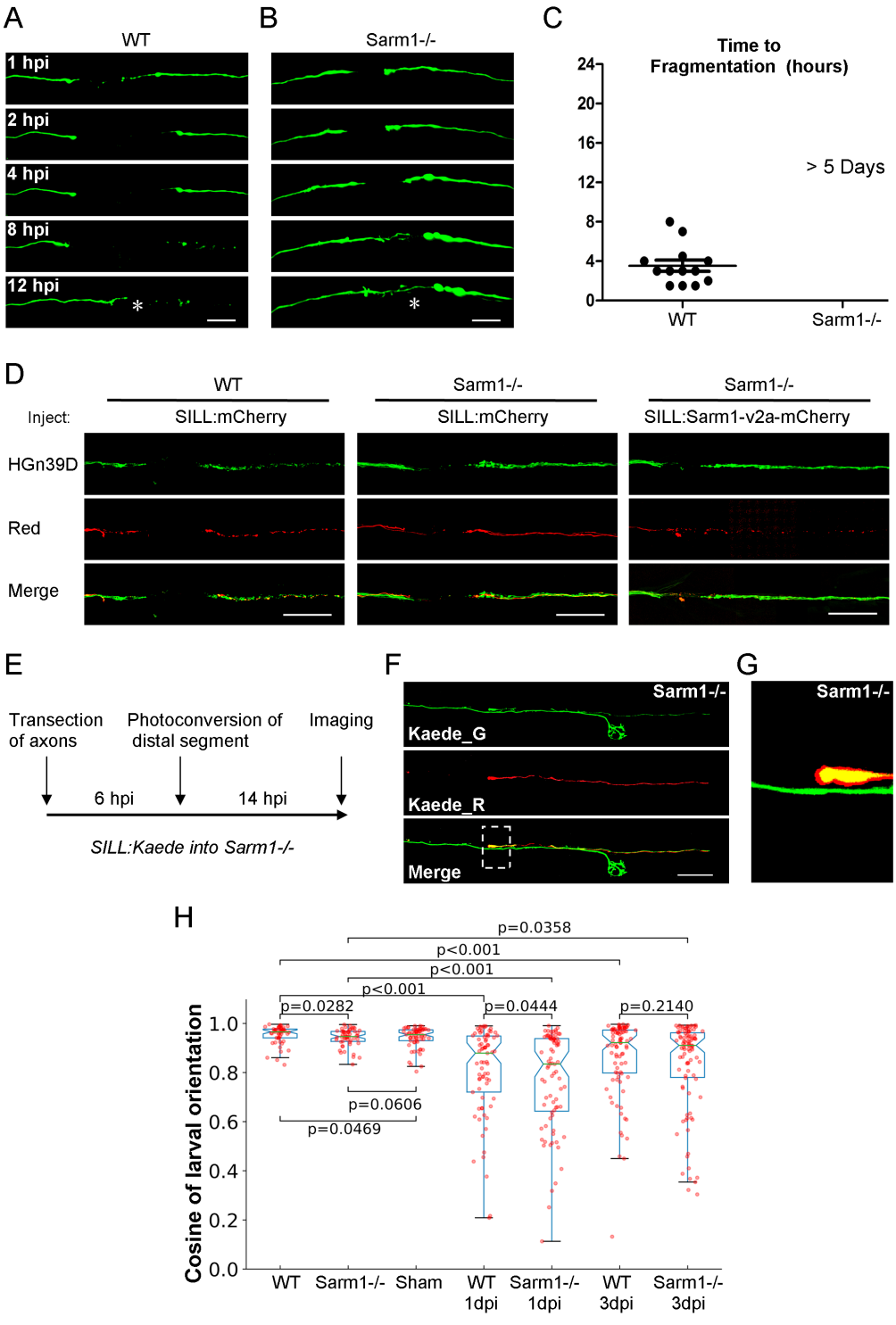

Figure 4. A-B) Time-lapse images of axonal degeneration of GFP-labeled lateralis sensory neuron in wild-type (A) and Sarm1-/- larvae (B). hpi=hour post injury, scale bar=50μm, white asterisk indicates the regrowing axons from the proximal stump. **C)**

Quantification of the time from axon transection to fragmentation in wild type (n=13) and Sarm1-/- (n=13). **D)** Confocal images of a severed lateralis nerve in the *Tg[HGn39D]* transgenic line (green) that also expresses mCherry in a fraction of axons in a wild-type (left) and a Sarm1-/- larva (center). The images on the right show a Sarm1-/- larva in which the red axons express a fusion between a functional Sarm1 and mCherry, revealing degradation of red axons and maintenance of green axons. Scale bar 100μm. **E)** Schematic representation of the experimental strategy to test the axon resealing in Sarm1-/- transected axons expressing Kaede. Photoconversion of distal segment was performed 6 hours post injury (hpi), and imaging 14 hours afterwards. **F)** Confocal images of the photoconversion experiment. Kaede_G is the green (native) form of Kaede, in the proximal (regrowing) axon; Kaede_R is the red (photoconverted) form of Kaede in the non-degradable (distal) axon segment. Scale bar 40μm. The dotted box indicates the site of transcetion, which also contains the juxtaposition between the proximal end of the distal axon segment and the passing regenerated axon. Note the arborization of the green axon below a neuromast. **G)** Zoomed are from the dotted box in (F), detailing the interphase between the non-degradable distal axon (orange) and the passing regenerated proximal axons (green). **H)** Rheotaxis of 7dpf larva in the indicated groups. Sham: sham ablation of the lateralis nerves. 1dpi: 1 day post injury; 3dpi: 3 day post injury. p value were from the Wilcoxon rank sum test. n=7 for each group, 10 trails for each larva.

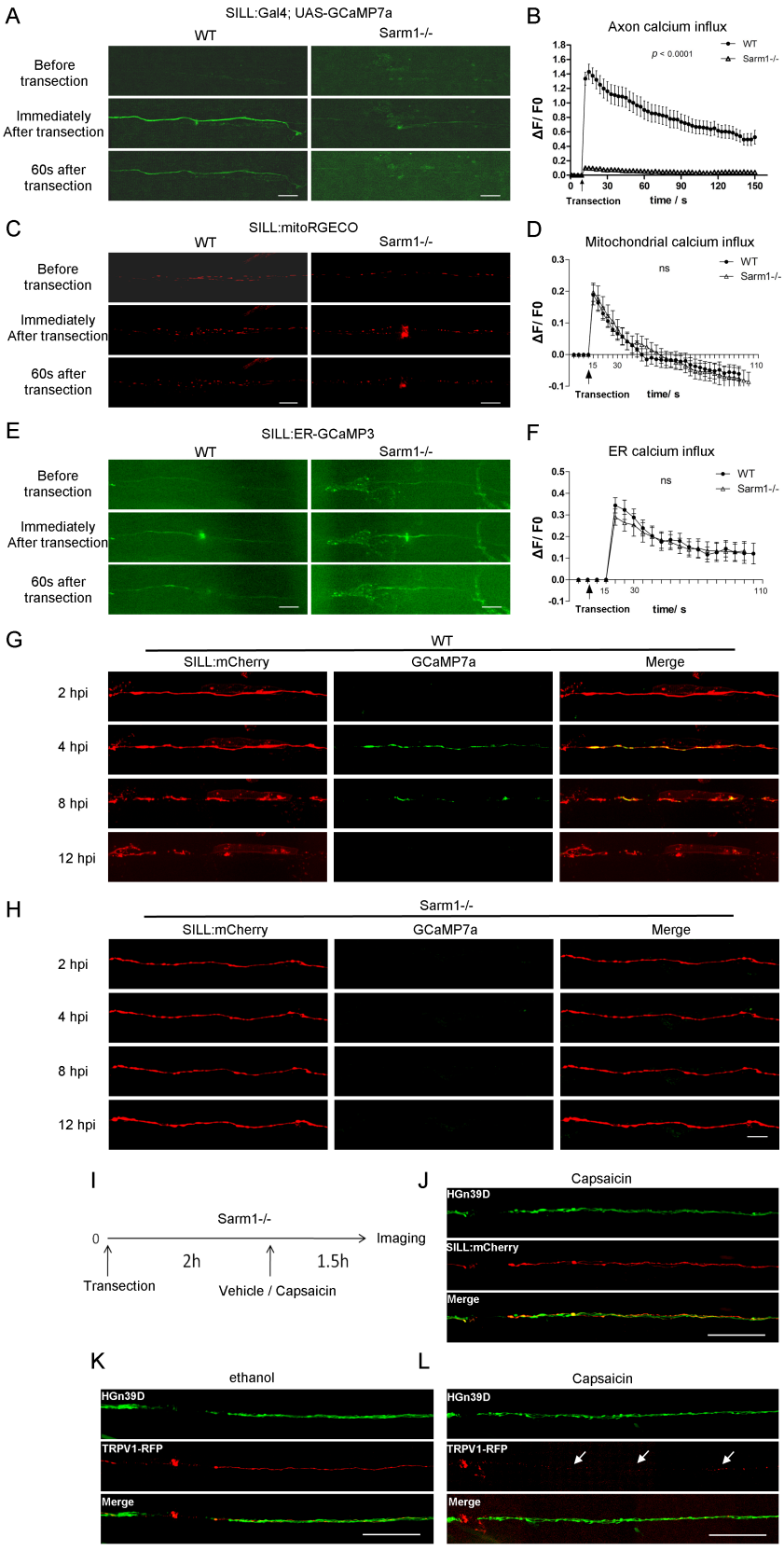

Figure 5. A) Confocal image of a single lateralis sensory axon expressing the green-fluorescent calcium sensor GCaMP7a in wild type (left column) and Sarm1-/- fish (right column). Rows show that same samples before laser-mediated transection (top), immediately after transection (middle) and 60 seconds after transection (bottom). Scale bar 20µm. **B)** Shows quantification of the first wave of axoplasmic calcium. Data are shown as mean ± SEM; p from one-way ANOVA, wild type n = 16, Sarm1-/- 16. **C)** Shows a confocal image of lateralis sensory axons expressing the red-fluorescent calcium sensor RGECO in wild type (left column) and Sarm1-/- fish (right column). Rows show that same samples before laser-mediated transection (top), immediately after transection (middle), and 60 seconds after transection (bottom). **D)** Quantification mitochondrial calcium influx shows the strong and nearly identical elevation and decay in wild type and Sarm1-/- immediately after the cuts. Data are shown as mean ± SEM; p from one-way ANOVA, wild type n = 16, Sarm1-/- 16. **E)** Shows a confocal image of lateralis sensory axons expressing the green-fluorescent calcium sensor CCaMP3 targeted to the endoplasmic reticulum (ER) in wild type (left column) and Sarm1-/- fish (right column). Rows show that same samples before laser-mediated transection (top), immediately after transection (middle), and 60 seconds after transection (bottom). **F)** Quantification ER calcium influx shows strong and statistically equal elevation and decay in wild type and Sarm1-/- after the cuts. Data are shown as mean ± SEM; p from one-way ANOVA, wild type n = 16, Sarm1-/- 16. **G)** Confocal image of a lateralis sensory axons expressing the mCherry (red) and green-fluorescent calcium sensor GCaMP7a (green) in wild type fish. Rows show same axons 2, 4, 8 and 12 hours after transection (hours-post-injury = hpi). **H)** Confocal image of lateralis sensory axons expressing the mCherry (red) and green-fluorescent calcium sensor GCaMP7a (green) in Sarm1-/- fish. Scale bar 20µm. **I)** Schematic representation of the experimental strategy to synthetically elevate calcium in Sarm1-deficient transected axons. Lateralis sensory neurons were made to express a transgene coding for the rat transient receptor potential cation channel subfamily V member 1 (TrpV1) fused to RFP, or simply mCherry. Two hours after axon transection, zebrafish larvae were bathed in ethanol solution (control), or ethanol containing

capsaicin, a natural activator of TrpV1. 90 minutes after treatments, larvae were imaged by confocal microscopy to assess the extent of distal segment degradation. **G)** Sarm1-/- fish expressing GFP in all lateralis neurons (*Tg[HGn39D]*) and mCherry in a mosaic manner in some neurons. Scale bars 100μm. **K)** Sarm1-mutant fish expressing GFP in all lateralis neurons and TrpV1-RFP in a mosaic manner. Scale bars 100μm. **L)** Sarm1-mutant fish expressing GFP in all lateralis neurons and TrpV1-RFP in a mosaic manner. Capsaicin treatment induced transected axon degradation (former location of the axon signaled by three white arrows). Scale bars 100μm.

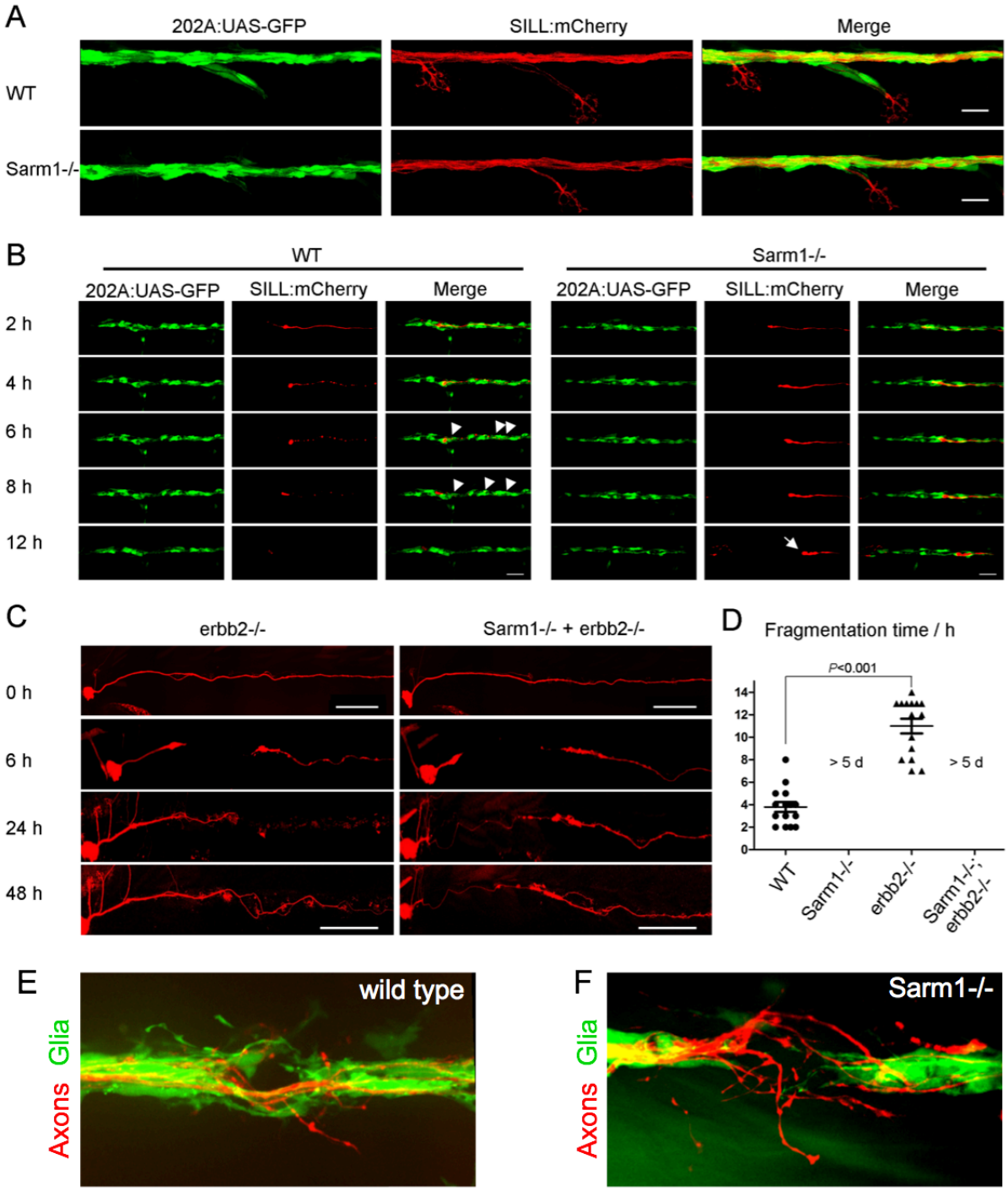

Figure 6. A) Confocal images of a double transgenic 5dpf larva showing Schwann cells marked by expression of GFP (green) under the control of the *Tg[gSAGFF202A]* Gal4 driver, and lateralis afferent neurons marked by expression of mCherry under the control of the SILL enhancer (red). Wild type (top), Sarm1 mutants (bottom). Scale bar 20µm. **B)** Images show the indicated time points after axon transection (hours post injury = hpi) from a videomicroscopic recording of Schwann cells (green) and

their interaction with axons (red) in wild-type and Sarm1-/-. White arrowheads indicate Schwann cells engulfing axonal debris in the wild type. A white arrow indicates degradation-resistant axon segment in Sarm1-/-. Please, note that the proximal axon stump in Sarm1-/- is not visible in these images because it is outside the focal plane. **C)** Images of mCherry-expressing (red) transected axons in Erbb2-/- mutants and Sarm1-/- ; ErBb2-/- double mutants. Scale bar 100μm. **D)** Quantification of transected axon fragmentation in Erbb2-/- and Sarm1-/-; ErBb2-/-. Error bar = SEM, p value from One-way ANOVA test, n = 15 (each group). **E)** Image of a from Supplemental Movie 1, showing the discrete local defasciculation of regenerated the sensory fiber (red) and the bridging of the glial gap by Schwann cells (green) in a wild-type specimen. **F)** Equivalent experiment, taken from Supplemental Movie 2, showing a more pronounced local defasciculation of the regenerated the sensory fiber (red) in a Sarm1-mutant specimen. Note that and the bridging of the glial gap does not occur.

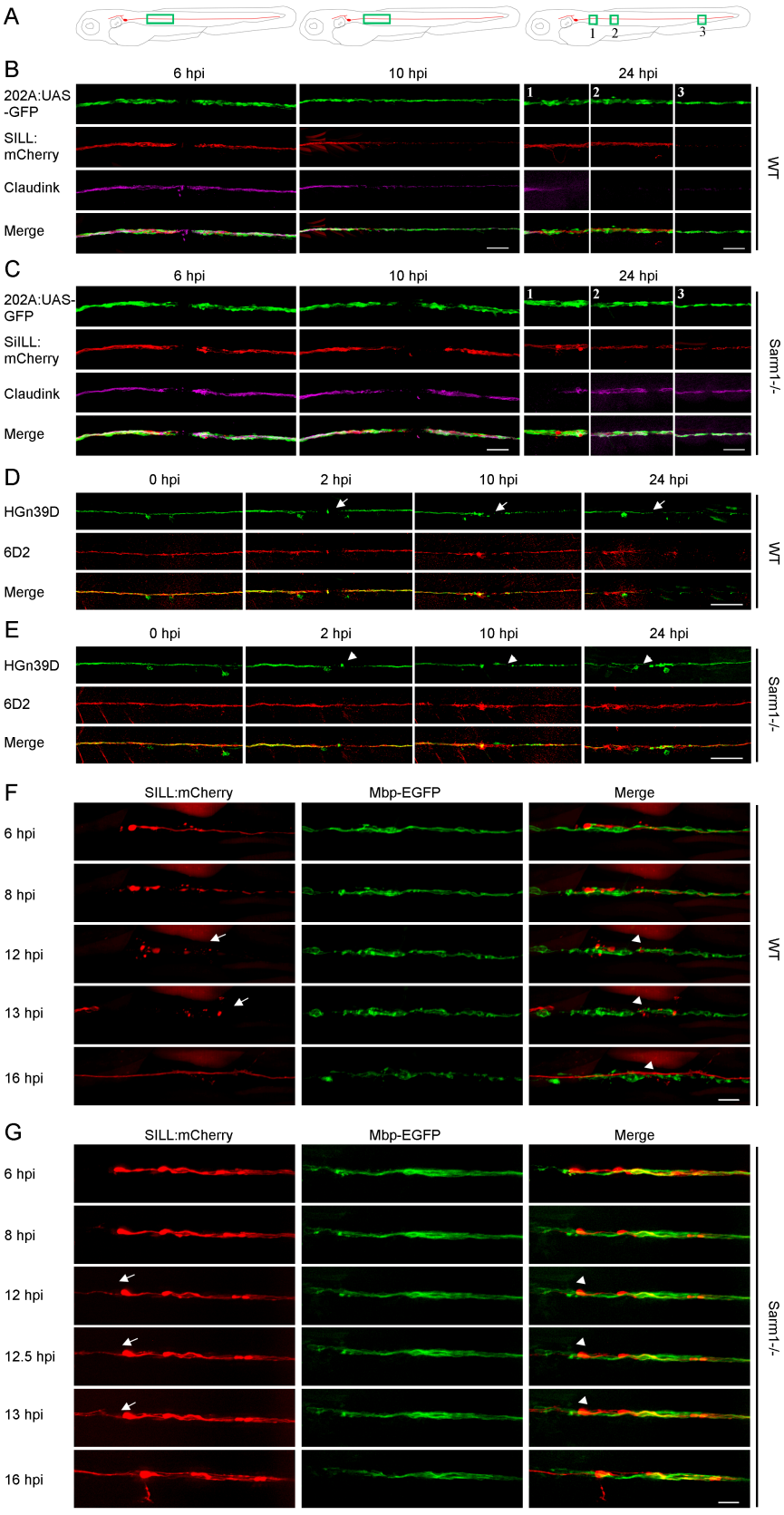

Figure 7. A-C) Schematic model of the confocal imaging locations on severed axons (A). Confocal images of wild type (B) and Sarm1-/- (C) specimens in 6hpi, 10hpi and 24hpi. hpi = hour post injury. The specimens were the *Tg[gSAGFF202A;UAS:EGFP; SILL:mCherry]* lines and were stained with Claudin-k (magenta) antibody. Scale bar 50μm. **D-E)** Confocal images of wild type (D) and Sarm1-/- (E) specimens expressing EGFP in sensory neurons of the lateral line (green) and stained with the monoclonal antibody 6D2. Stainings were performed at indicated time points after axons severing (hpi). The arrows point to the cutting sites. Scale bar is 50μm. **F)** Live imaging of the *Tg[Mbp-EGFP; SILL:mCherry]* after severing. The arrows indicated the fragmented axons and the arrowheads the fragmented myelin. Scale bar 20μm. **G)** Live imaging of the Sarm1-/- in *Tg[Mbp-EGFP; SILL:mCherry]* after severing. Arrows indicate regrowing axons, and arrowheads indicate the juxtaposition between the regrowing axons. Scale bar 20μm.

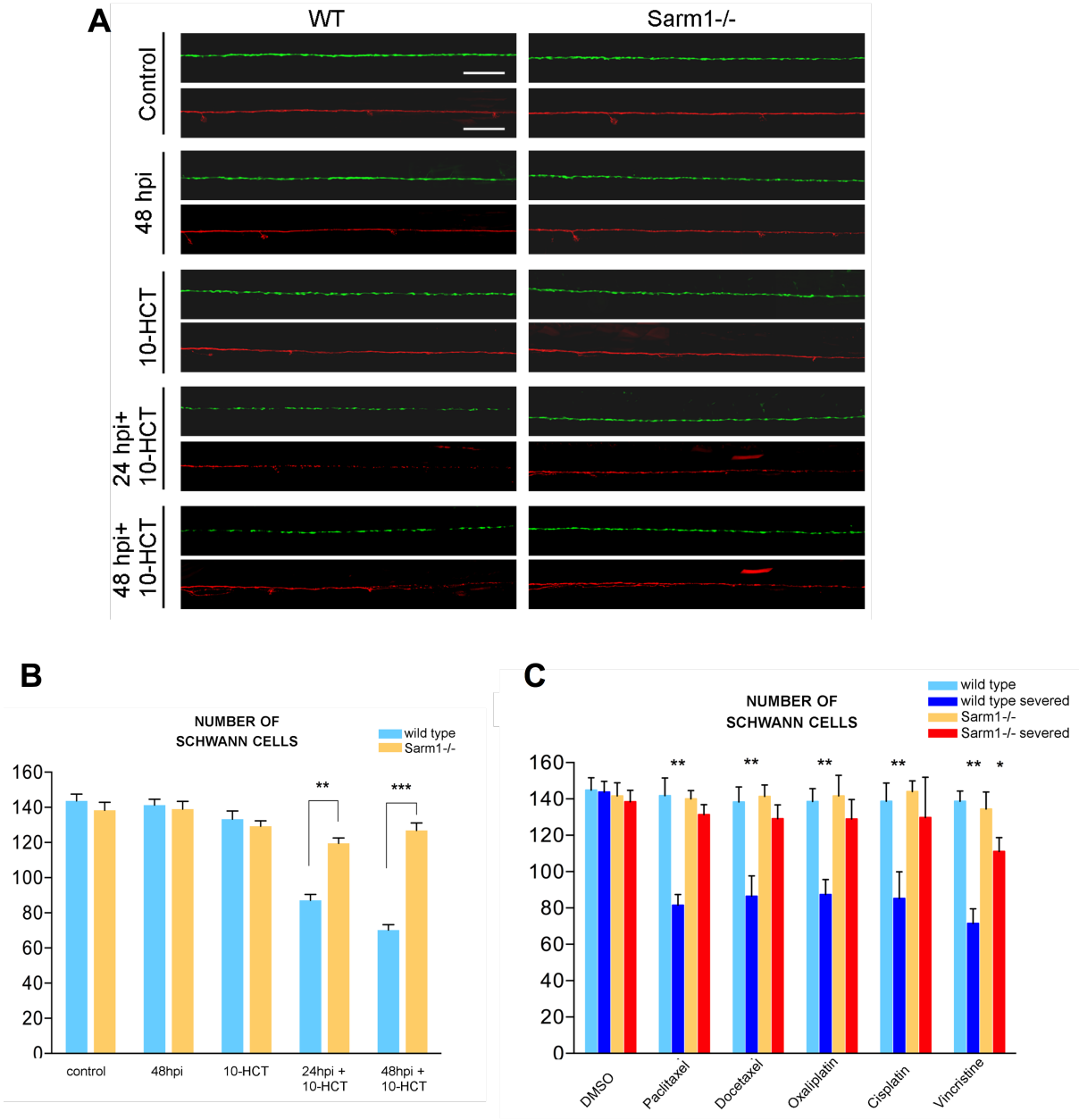

Figure 8. A) Confocal images showing Schwann cells (green) and lateralis sensory axons (red) in a control specimen (in which axons were not transected), in a specimen 48 hours after axon transection, and in specimens treated with 10-HCT (10-Hydroxycamptothecin). Left column is wild type and right column shows Sarm1-/-. In all cases, the concentration of 10-HCT in water was 40μm. Scale bar 100μm. **B)** Quantification of the Schwann cells from A). Data are shown as mean ± SEM. ** means $p < 0.01$, one-way ANOVA, $n = 8$ (each group). **C)** Quantification of Schwann cells of WT, WT severed, Sarm1-/- and Sarm1-/- severed with the treatment of the indicated chemical compounds for 48 hours. Concentrations:

Paclitaxel 40μm, Docetaxel 0.1μm, Oxaliplatin 500μm, Cisplatin 50μm, Vincristine 50μm. Data are shown as mean ± SEM. * means $p < 0.05$; ** means $p < 0.01$, one-way ANOVA, n = 8 (each group).

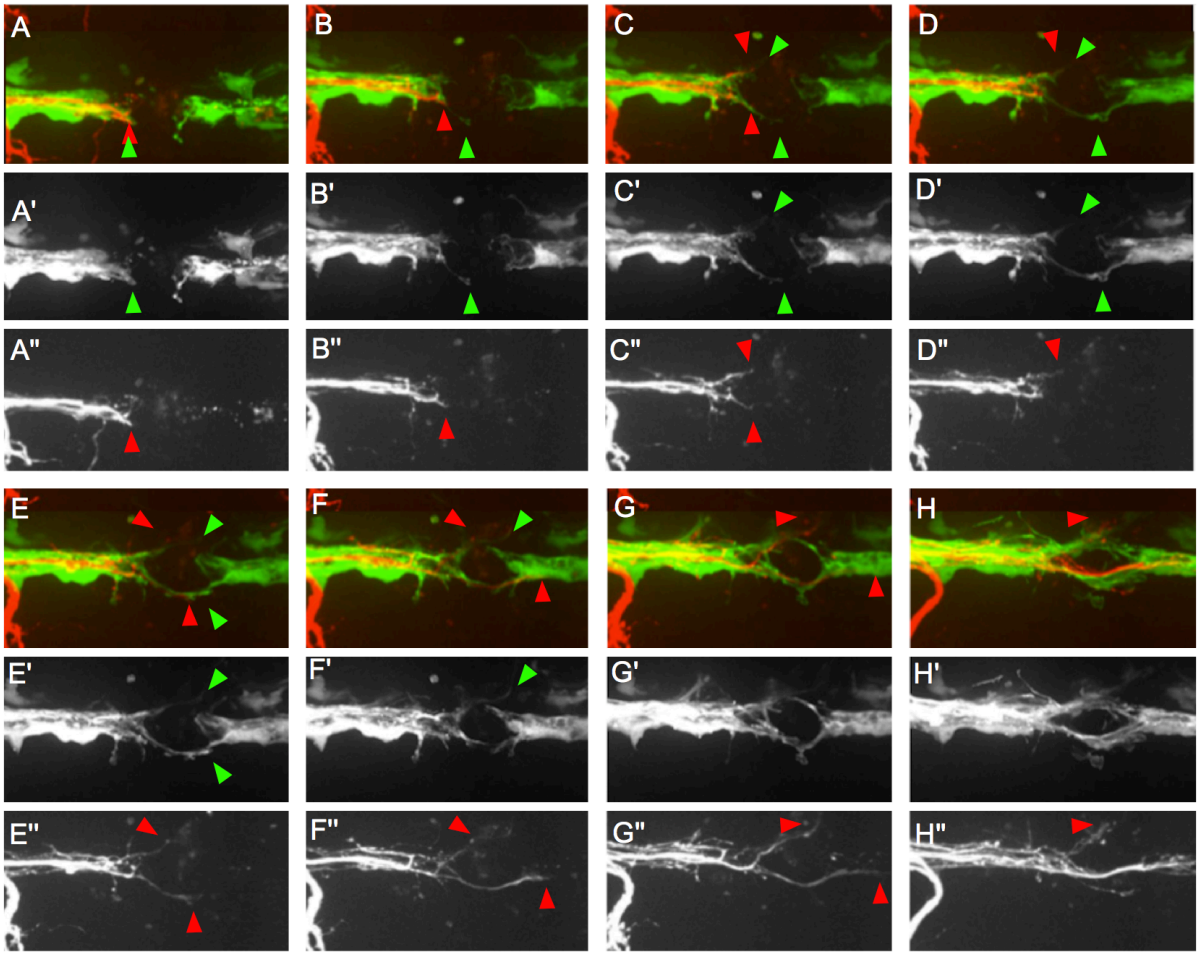

Supplemental Figure 1. Series of still images taken from Supplemental Movie 1 (also shown in Figure 6, panel E). They show eight time points during the repair of the gap in the glial scaffold (A'-H') and axonal regeneration after transection (A"-H") in a wild-type animal. Rostral is left and caudal is right. In all panels, the red arrowheads signal the location of the pioneering growth cone of the regenerating axons. The green arrowheads mark the filopodia-like extensions from Schwann cells adjacent to the glial

gap. At the start of the series, the axonal terminal stump and the Schwann cells proximal to the gap co-localize (juxtaposition of the green and red arrowhead). In C', a Schwann cell extends a filopodium across the gap, whereas the axons (C'') do not grow along this extension of across the gap. In D', several extensions from Schwann cells are clearly visible at the top and bottom aspects of the image. The shape of the lower extension from a Schwann cell did not change shape, suggesting that they are stabilized, perhaps through interactions with the substrate. Proximal axons (D'') start to grow along these Schwann-cell protrusions. In E', the extensions from the anterior and posterior Schwann cells have crossed the gap, physically interact and commence to reconstitute a continuous glial scaffold. The axonal projections (E''), however, have suffered a retraction towards the proximal stump. F'-H' show a continuation of Schwann cells behavior, increasing the contacts and closing the gap, which is obvious by the smaller area of the gap (distance between proximal and distal Schwann cells). F''-H'' show a more robust and persistent extension of the axonal growth cones, which grow nearly strictly along the Schwann cells extensions. Although the gap in the glial scaffold is much reduced, nerve fibers show discrete defasciculation (H'').

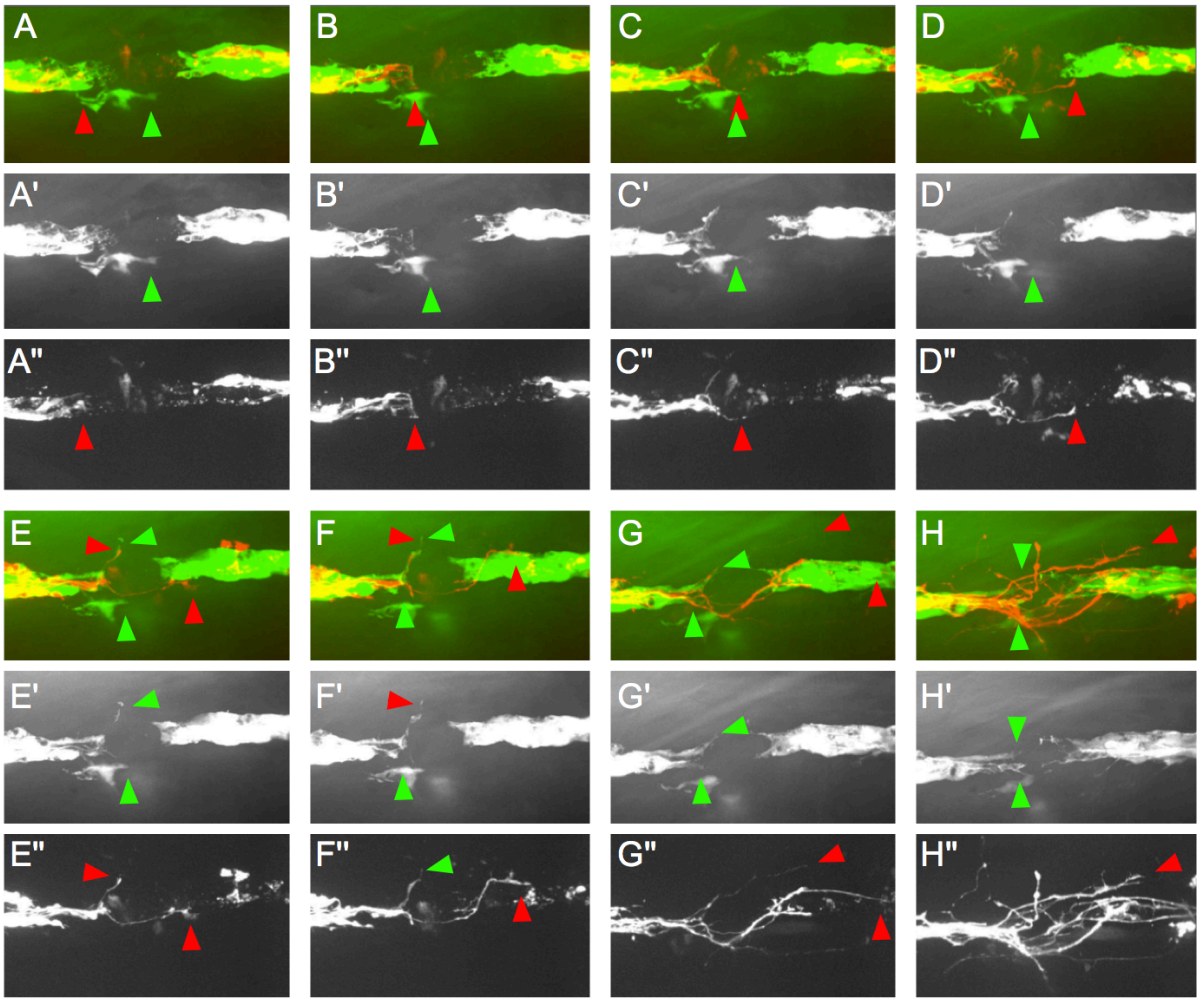

Supplemental Figure 2. Series of still images taken from Supplemental Movie 2 (also shown in Figure 6, panel F). They show eight time points during the repair of the gap in the Schwann-cell scaffold (A'-H') and axonal regeneration after transection (A''-H''), in a Sarm1-mutant specimen. In all panels, the red arrowheads signal the location of the pioneering growth cone of the regenerating axons, and the green arrowheads mark filopodia-like extensions from Schwann cells. Unlike the wild-type situation shown in Supplemental Figure 1, the Schwann cells adjacent to the gap form small filopodia-like extensions, but which never cross the gap. The proximal axon stumps eventually form growth cones that cross the gap at various locations and, upon finding distal Schwann cells, grow along the glial scaffold (E''-H''). Nerve fibers show extensive local defasciculation (H'').

Supplemental Movie 1. Videomicroscopic imaging of a 4dpf wild-type specimen carrying three transgenes Tg[SILL:mCherry; gSAGFF202A; UAS:EGFP], showing the dynamics of axons and Schwann cells after axonal transection. Sensory axons are shown in red and Schwann cells in green. The movie is a maximal projection of confocal stacks. It was recorded during 12 hours with a 10 minutes interval between image stacks. The top panel shown the merged images, the middle panel the Schwann cells, and the bottom panel the axons.

Supplemental Movie 2. Identical experiment as shown in Supplemental Movie 1, but conducted in a Sarm1-mutant specimen. It was recorded during 12 hours with a 10 minutes interval between image stacks. The top panel shown the merged images (SILL:mCherry; gSAGFF202A; UAS:EGFP), the middle panel the Schwann cells (gSAGFF202A; UAS:EGFP), and the bottom panel the axons (SILL:mCherry).

METHODS

Zebrafish strains and husbandry

Zebrafish (*Danio rerio*) were maintained in a centralized facility in accordance to guidelines by the Ethical Committee of Animal Experimentation of the Helmholtz Zentrum München, the German Animal Welfare act Tierschutzgesetz §11, Abs. 1, Nr. 1, Haltungserlaubnis, to European Union animal welfare, and to protocols number Gz.:55.2-1-54-2532-202-2014 and Gz.:55.2-2532.Vet_02-17-187 from the "Regierung von Oberbayern", Germany. The transgenic lines Tg[UAS:EGFP], Tg[HGn39D] and Tg[SILL:mCherry] (75), Tg[gSAGFF202A] (41), Tg[UAS:GCaMP7a] (68), Tg[mbpa:tgRFP-CAAX]^{tum102Tg} (also known as Tg[MBP:TGRFP]) (101) and Erbb2 mutants (41, 76) have been previously published. The Tg[Sarm1-/-] was generated by CRISPR/Cas9 mediated mutagenesis (see below) (102) (102) (102) (100) (100) (100) (100) (99) (99) (99) .

Sarm1 mutagenesis

We used CRISPR/Cas9-mediated genome modification to generate loss-of-function mutations in exon 1 of Sarm1. Cas9 mRNA and sgRNAs were co-injected into one-cell stage embryos. Cas9 mRNA was generated *in vitro* from PmeI linearized CAS9 vector (pMLM3613) using the Ambion™ mMESSAGE mMACHINE T7 Kit. The mRNA was purified with the RNA easy kit (Qiagen). To generate the sgRNAs, the target exon was sequenced and the sequence information was used to design oligonucleotides for the sgRNA guide vector (pDR274) using the on-line tool "ZiFiT Targeter software package" (http://zifit.partners.org/) (103). The sgRNA sequence for exon 1 of Sarm1 is 5'-GGGACTTGGAAGAGACCCGC-3'. The annealed oligonucleotide was cloned into the BsaI-digested pDR274 vector using T4 ligase (NEB M0202). Resulting clones were sequenced to verify correctness, and then linearized with DraI. The purified linearized DNA fragment was employed to generate the sgRNA using the T7 MEGAscript kit (Ambion™). By out-crossing adult fish resulting from injection, we obtained germ-line transmission of two independent alleles: *sarm1*^{hzm13} and *sarm1*^{hzm14}. For genotyping mutant carriers, we used the primers: Forward: 5'-GATTTGCCGTTATCTCTCCA-3' and Reverse: 5'-TCAAGCAGTTTGGCAGACTC-3'.

DNA constructs

The DNA constructs SILL:mCherry, SILL:Gal4 (75), UAS:Synapsin1-GFP (53) and mbp:EGFP-CAAX(101, 104)(101, 104)(101, 104)(99, 102)(99, 102)(99, 102)(99, 102)(98, 101)(98, 101)(98, 101) have been previously described. The vectors pMLM3613 (42251) and pDR272 (42250) were purchased from Addgene. The plasmids UAS:TRPV1-tagRFP, the coding sequence of rat TRPV1 containing the E600K mutation fused to tagRFP was commercially synthesized by Genecat and the expression construct was generated using Tol2 kit. The constructs SILL:mito-mCherry, SILL:Sarm1-v2a-mCherry, SILL:Kaede, SILL:mitoRGECO and SILL:erGCaMP3 were generated using Tol2 kit. Mitochondria in lateralis neurons were marked by expressing the mitochondria targeting sequence from the Cytochrome-C oxidase subunit 8A fused to mCherry. The plasmids containing mito-

RGECO and er-GCaMP3 (105) were a gift of David W. Raible (University of Washington).

Antibodies and immunostaining

Whole-mount immunostaining was performed as following. First, samples of zebrafish embryos or larvae were fixed by immersion in ice-cold 4% paraformaldehyde diluted into phosphate-buffered saline buffer containing 0.2% Tween20 (PBST), and incubated overnight at 4°C. Then, the samples were washed at room temperature (RT) with PBST three times, 10 minutes per wash, and subsequently blocked in 10% bovine serum albumin (BSA), also at RT for 1 hour. Next, the samples were incubated in primary antibodies at 4°C overnight. Next, the samples were washed in PBST for 2 hours, changing to fresh buffer every 30 minutes. Finally, they were incubated with secondary antibodies at 4°C overnight. Primary antibodies and concentrations: mouse anti-Acetylated tubulin, 1:1000 (Sigma T7251); rat anti-Claudin-k, 1:500 (gift from Thomas Becker, University of Edinburgh, U.K.) (80); mouse 6D2, 1:5 (gift from Dr. Gunnar Jeserich, University of Osnabrück, Germany) (82). Secondary antibodies used were at the following concentrations: donkey anti-Mouse Alexa Fluor® 555, 1:200, Abcam ab150106; donkey anti-Rat IgG H&L (Alexa Fluor® 647) pre-adsorbed, 1:200, Abcam ab150155). Samples were washed in PBST for 30 minutes and mounted in Vectashield one day before microscopic examination. Imaging of fixed samples was done with a laser-scanning confocal microscope (LSM 510, Carl Zeiss).

Intravital microscopy

For videomicroscopy, larvae were anesthetized with MS-222 (0.013% M/V) in Danieau's and mounted in 0.8% low melting-point agarose on a 35mm glass-bottom Petri dish. Samples were gently pressed against the glass using a hair-loop glued to the tip of a glass pipette, as previously described. The agarose dome was immersed in Danieau's with the anesthetic. Images of the axons and Schwann cells were acquired using a spinning-disc microscope with a 40× air objective at 28.5°C (63). Z-stacks were set to 0.8-1.2 µm intervals. Time intervals were 10 minute or 15 minute per stack. The resulting raw data were processed, assembled and analyzed with ImageJ.

Western blot assay

Wild-type and mutant larvae were anesthetized and killed 5 days-post-fertilization. Samples were homogenized in ice-cold RIPA buffer (with protease inhibitor cocktail from Roche (Cat.04693159001). After homogenization, the samples were incubated on ice for 30 minutes for further lysis. The resulting lysate was centrifuged at 1200 rpm at 4°C, and the supernatant was taken for the BCA assay. The supernatant was diluted in loading buffer and boiled at 99°C for 5 minutes. Next, the samples were performed in the SDS-PAGE and transferred onto a PVDF membrane. After blocking the membrane in 5% skimmed milk (diluted in PBST) for 1 hour, the membrane was incubated with the primary antibody (rabbit anti-Sarm1, 1:500, ANASPEC 55381; Mouse anti-β-Tubulin, 1:2000, Sigma T5168) at 4°C overnight. The next day, the membrane was washed and incubated with HRP-labeled secondary antibody (Peroxidase-Affini Pure Goat Anti-Mouse IgG (H+L), 1:10000, Jackson Immuno Research 115035003; Peroxidase-Affini Pure Goat Anti-Rabbit IgG (H+L), 1:10000, Jackson ImmunoResearch 115035144) for 1 hour. Images were acquired by developing the membrane with ECL (Pierce™ ECL Western Blotting Substrate, Thermo Fisher, 32109).

Laser microsurgery

To mark lateralis sensory neurons individually, DNA of the SILL:mCherry construct was injected into eggs of Tg[HGn39D], Tg[HGn39D; Sarm1-/-], Tg[SILL:mCherry; gSAGFF202A; UAS:EGFP] or Tg[SILL:mCherry ; gSAGFF202A ; UAS:EGFP ; Sarm1-/-] zebrafish. Resulting larvae were selected according to red-fluorescence in lateralis neurons. Selected samples were mounted into agarose as described above, and their peripheral axons were targeted an ultraviolet laser (350nm) using the iLasPulse system (Roper scientific AS, Evry, France), as described previously. The laser beam was delivered using a 63x water-immersion objective (50, 53, 63). The laser pulses were calibrated and applied to the target area until a clear gap in the axons was visible. The samples were observed again 1 hour post-injury (hpi) to confirm that the axons were completely transected.

Quantification of mitochondrial density and motility

To analyze mitochondria in sensory axons, we generated kymographs of mito-mCherry fluorescent spots using the Multi-Kymograph tool of the Fiji software (http://fiji.sc). The movement of mitochondria was determined by the slope of the lines drawn over time, and the direction of movement was determined by the moving mitochondria crossing the time line (vertical) in the kymographs. The data were analyzed with Python scripts and the Graphpad Prism software.

Calcium imaging

For calcium imaging in lateralis neurons, Tg[SILL:Gal4; UAS:GCaMP7a] double-transgenic larvae were anesthetized and mounted in 0.8% low melting-point agarose on a 35mm glass-bottom Petri dish. Imaging was acquired through a 63x water-immersion objective with an exposure time of 400 milliseconds. Laser-mediated axon transection was done after the 4th imaging of the time series. Next, live videomicroscopy was done for 2 minutes at a frame rate of 400 milliseconds at 28.5°C. The raw data were analyzed with ImageJ. To quantify the calcium signal, the images were processed to ImageJ. The region of interest (ROI) was selected and measured the value with time point. GCaMP or RGECO intensity changes were calculated as follows: $\Delta F/F0 = (F–F0)/F0$, where F0 is the value of the fluorescent signal before axons were transected, and F is the value of the fluorescent signal with time point after axon severing (105).

Chemogenetics

For chemogenetic experiments, we co-injected the SILL:Gal4 with UAS:mCherry or UAS:ratTRPV1-tagRFP into the Tg[UAS:GCaMP7a] or Tg[HGn39D; Sarm1-/-]. The positive larva with SILL:Gal4; UAS:ratTRPV1-tagRFP; UAS:GCaMP7a expression was used to activate TRPV1 channels in zebrafish by incubation in 5μM capsaicin (Sigma, M2028) and subsequent live imaging for 1hour of the mounted and anesthetized embryo. Images were acquired through a 63x water-immersion objective with an exposure time of 400 milliseconds. For experiments with the Sarm1 mutant larvae, the HGn39D with SILL:mCherry or ratTRPV1-tagRFP positive animals were laser axotomized. The larvae were treated with 10 μM capsaicin or ethanol (1:1000,

v/v) 2h after transection. 1.5h after capsaicin treatment, images were taken by spinning disc microscopy.

Electrophysiological recordings

Recordings were performed as previously described, with some modifications (49, 50, 54). Briefly, 4-5 dpf larvae were anaesthetized in 0.03% Tricaine solution and paralyzed in 0.1% α-bungarotoxin (Molecular Probes). Samples were rinsed and mounted laterally with tungsten pins on Sylgard lined dishes. Recordings of action potentials in lateralis afferent neurons were made in extracellular solution (NaCl 134 mM, KCl 2.9 mM, MgCl2 1.2 mM, HEPES 10mM, Glucose 10 mM, pH 7.8, 290 mOsm), under an Axioskop microscope (Zeiss) modified to a fixed-stage set-up, using DIC optics. Action potentials were recorded in loose patch configuration from afferent neurons of the posterior lateral line with borosilicate glass pipettes pulled (Sutter P-2000) to a resistance of 3.5-6 MΩ in extracellular solution. Data were acquired with a Multiclamp 700B amplifier and a Digidata 1440A digitizer using pClamp10 software (Molecular Devices). Recordings were made in current clamp mode, sampled at 20 kHz and filtered at 1kHz. Direct mechanical stimulation of hair cells was achieved using a water jet from a glass micropipette (tip diameter ~ 30µm) driven by a pressure pump (ASI MPPI-3) triggered by a voltage output signal from the Digidata 1440A. The stimulation pipette was positioned parallel to the fish trunk along the midline in proximity to a neuromast. Neuromasts were sequentially stimulated with a test pulse until an evoked response was detected. Once a response was detected, 20 pressure pulses were applied during 5 second long sweeps, with one-second delay and 100-milisecond duration. Spontaneous spike rate was recorded before stimulation during 12-120 seconds. Spike rate before each stimulus was calculated during the first 200 milliseconds of a recording sweep and evoked spikes were calculated from spikes during 200 milliseconds after stimulus onset. Latency was measured as the first spike after stimulus onset. Spike rate and latency were averaged from 20 stimulations for each recording. Spike detection from recordings was done in DataView (Version 11.0, W. Heitler, University of St. Andrews) by setting a negative threshold at 4X the

standard deviation of the first 1000 milliseconds of the recording. Further data analysis and statistics were performed using Matlab (Version 8.6 R2015b).

Behavioral assays

For the touch-mediated escape response, 2dpf embryos were gently dechorionated and kept in Danieau's solution at 28ºC for at least 1 hour. Embryos were place into a flat uncovered Petri dish containing Danieau's and were recorded with a high-speed camera (NX4 series, Imaging solution, GmbH). Video recording was launched and a randomly chosen embryo was touched with a blunt glass needle until it evoked a reaction. Recordings were done under white-light illumination over 150 seconds at a rate of 200 frames per second (fps). The swimming trajectories were obtained with 3D Particle Tracker plugin, ImageJ software. The further quantification and statistics were using Python. For rheotaxis, a behavioral rig was designed to evaluate zebrafish orientation to the direction of water flow under laminar conditions in darkness and in isolation from significant environmental noise, as previously described (56). The rig was constructed of a Plexiglas® pipe with inner diameter of 2.4 cm filled with the water. One side of the pipe is connected to the water reservoir and in the other side is the plunger connected to the motor shaft. Movement of the motor shaft displaces the plunger back and forth causing the water flow inside the tube. The rig was illuminated with an infrared light-emitting diode (LED) array (IR: 940 nm) (56). Images of fish movement were captured with a high-speed camera (NX4 series, Imaging solution, GmbH) at 200 frames per second (fps). Captured images were saved in the computer hard drive for further analysis. Animal tracking and orientation analysis were done using the Bonsai software. For each experiment, the test fish were placed and kept in the rig for 30 minutes prior to the experiment. A pause of 5-10 minutes with zero flow was followed by each trial. The orientation of the fish relative to flow direction was used to derive a rheotactic performance.

Statistical analysis

The Student's t test (two tailed), one-way ANOVA test and Wilcoxon rank sum test were applied using Python scripts. Error bars in all figures are standard errors of the mean (SEM).